BIROn - Birkbeck Institutional Research Online

Tian, Y. and Liu, Y. and Sun, X. and Zhang, Z. and Carter, Andrew and Vermeesch, Pieter (2022) Thermochronological constraints on Eocene deformation regime in the Long-Men Shan: implications for the eastward growth of the Tibetan Plateau. Global and Planetary Change 217 (103930), ISSN 0921-8181.

Downloaded from: https://eprints.bbk.ac.uk/id/eprint/52041/

Usage Guidelines:
Please refer to usage guidelines at https://eprints.bbk.ac.uk/policies.html or alternatively contact lib-eprints@bbk.ac.uk.

Thermochronological constraints on Eocene deformation regime in the Long-Men Shan: Implications for the eastward growth of the Tibetan Plateau

Yuntao Tian [a,b], Yimin Liu [a], Rui Li [a], Xilin Sun [a], Zengjie Zhang [a], Andrew Carter [c], Pieter Vermeesch [d]

[a] Guangdong Provincial Key Lab of Geodynamics and Geohazards, School of Earth Sciences and Engineering, Sun Yat-sen University, Guangzhou 510275, China

[b] Southern Marine Science and Engineering Guangdong Laboratory, Zhuhai, China

[c] Department of Earth and Planetary Sciences, Birkbeck, University of London, London, UK

[d] Department of Earth Sciences, University College London, London, UK

Corresponding author information:

Yuntao Tian

School of Earth Sciences and Engineering, Sun Yat-sen University, Guangzhou, China

Email: tianyuntao@mail.sysu.edu.cn

ABSTRACT

Understanding the spatio-temporal distribution of strain during Cenozoic growth of the Tibetan Plateau is important for constraining the geodynamic processes underpinning plateau formation. Offset Quaternary landforms and historic earthquake data suggest an along-strike change in deformation style for the eastern margin of the Tibetan Plateau, characterized by a transition from SEE-verging shortening to right-lateral shear from the southern to northern segment of the Long-Men Shan fault zone within a distance of ca. 500 km. When and how this along-strike deformation pattern formed is central to understanding the uplift history and spatio-temporal distribution of strain in the eastern margin of the Tibetan Plateau, and the underpinning geodynamics. To address this, we report a suite of low-temperature thermochronology data from the northern segment of Long-Men Shan fault zone that show a contrast in post late Cretaceous cooling and exhumation histories between the hinterland (west of the marginal Yingxiu-Beichuan fault) and foreland sides (east of the fault). Prior to the Eocene (ca. 40 Ma) the hinterland experienced significant exhumation in contrast to minor exhumation on the foreland side but, post Eocene exhumation accelerated on the foreland side. This change reflects a switch in the deformation regime from shortening to strike-slip-dominated. This switch reduced hinterland rock uplift and tectonic and topographic loading over the foreland basin, leading to accelerated foreland exhumation through isostatic adjustments. A compilation of fault deformation history for the eastern Tibetan Plateau shows a second tectonic transition in the late Miocene, characterized by formation of the south-striking Huya and Minjiang faults. Our results highlight the importance of progressive late Eocene and late Miocene tectonic transitions in shaping the eastern margin of the Tibetan Plateau.

Keyword: Low-temperature thermochronology, Tibetan Plateau, Tectonic transition, Exhumation, Plateau growth

1. Introduction

The Tibetan Plateau, the world's highest and largest orogenic plateau, resulted from a series of continental accretions and collisions during the Mesozoic and Cenozoic (Powell and Conaghan, 1973; Chang et al., 1986; Yin and Harrison, 2000). Ongoing convergence between the Indian and Eurasian plates has continued to drive plateau expansion (Tapponnier et al., 2001; Royden et al., 2008; Wang et al., 2008; Molnar et al., 2010), albeit mainly in a northerly and easterly direction. Along the eastern margin related structures are defined by the SW-striking Long-Men Shan fault zone (LMSFZ) where the crust is ca. 60-65 km thick, some 20 km thicker than the adjacent Sichuan foreland basin (e.g., Zhang et al., 2009). The eastern margin also has one of the steepest intra-continental scarps, where, within a 50 km distance, elevations drop from peaks exceeding 5 km to ca. 500 m in the adjacent Sichuan Basin (Fig. 1c and 1d).

The eastern plateau margin has been regarded as a natural laboratory for understanding the geodynamic mechanisms responsible for growth of the Tibetan Plateau (Burchfiel et al., 1995; Chen & Wilson, 1996; Kirby et al., 2002; Royden et al., 2008; Hubbard and Shaw, 2009; Wang et al., 2012; Tian et al., 2013; Jiang et al., 2019), but these continue to be debated. Previous models include upper crustal shortening (Hubbard and Shaw, 2009; Tian et al., 2013, 2015; Tan et al., 2019), lower crustal thickening and flow (Clark et al., 2005a; Royden et al., 2008), simple-shear shortening of the lithosphere (Yin, 2010) or crust (Guo et al., 2013), pure-shear deformation of the lithosphere (Yin, 2010), reactivation of pre-existing structures by transpressional shear (Sun et al., 2018), and progressive deformation evolving from early Cenozoic transpressional shortening to late Cenozoic lower crustal expansion (Zhang et al., 2022).

Geodynamic models for the formation of the eastern margin of the Tibetan Plateau should be compatible with structural variations seen along-strike the LMSFZ. Studies suggest that along the southern segment of the LMSFZ, east-verging shortening accompanied the development of an early Cenozoic foreland basin (southwest Sichuan Basin) (Jia et al., 2006; Tian et al., 2016). This shortening has been episodically reactivated through to the present-day, as shown by late Miocene enhanced rock exhumation, whose spatial variation is correlated with reverse faulting (Tian et al., 2013), and coeval parallel folds and thrusts in the foreland (Jia et al., 2006; Hubbard and Shaw, 2009). Ongoing shortening is responsible for recent earthquakes such as the 2013 M. 6.9 Lushan earthquake (Xu et al., 2013). To the north, in the central segment of the LMSFZ, structural analyses (Wang et al., 2014), offset landscape markers (Densmore et al., 2007; Godard et al., 2010), and the 2008 M. 7.9 Wenchuan Earthquake and associated aftershocks (Xu et al., 2009; Yu et al., 2010; Zhang et al., 2010; Zhang et al., 2015) indicate that deformation is characterized by eastward shortening, accompanied by a right-lateral component of slip. It remains unclear when these along-strike variations in deformation first initiated although a growing number of structural, magnetic fabric and Ar-Ar geochronology studies suggest a shortening regime existed in both the southern and central segments of the LMSFZ since the early Cenozoic, or even earlier (Xu et al., 1991; Dirks et al., 1994; Chen and Wilson, 1996; Burchfiel et al., 1995; Kirby et al., 2002; Tian et al., 2016; Xue et al., 2017; Airaghi et al., 2018; Yan et al., 2011; 2018). A better understanding of the structural evolution of the LMSFZ would provide new constraints for understanding strain migration history along the major faults that define the eastern Tibetan Plateau. These include the LMSFZ, Huya, Minjiang and East Kunlun faults (Tazang and Bailongjiang branches) (Fig. 1).

This work focuses on the little studied northern part of the LMSFZ, where prominent right-lateral features have been reported (Figs. 2 and 3). We present new thermochronological data from a ca. 150-km-long surface transect that spans the hinterland to foreland sides of the plateau margin. These data provide new constraints on the rock cooling and exhumation histories, which are used to reconstruct the evolution of strain and deformation across the area and the pattern of strain migration among major faults over a broader region. Together with a compilation of previous earthquake and seismic imaging results, we show how the northern segment of LMSFZ experienced a transition from upper crustal shortening to right-lateral shear in the Eocene and how strain migrated across the eastern Tibetan Plateau. Our findings have important implications for the evolution and geodynamics of the eastern Tibetan Plateau margin.

2. Topographic and geological setting

The elevation and slope of the northern segment of the LMSFZ, our study area, are significantly lower than the southern and central segments (Figs. 1b, 1c). Topographic swaths, calculated using 90 m resolution Shuttle Radar Topography Mission (SRTM) digital elevation model with a swath-width of 10 km, show that elevations increase from ca. 600 m in the western Sichuan Basin to peak elevations at ca. 4000 m in the northern segment of LMSFZ over a distance of ca. 95 km (Fig. 1c), with a topographic gradient of ca. 3%. In contrast, topographic gradients along the southern and central segments are ca. 10% (Kirby et al., 2002; Zhang et al., 2011) (Fig. 1d).

The LMSFZ shares common borders with the E-W striking Qinling orogen to the north, the rhombic Sichuan Basin to the east and the Songpan-Ganze terrane to the west (Fig. 1a). The area has experienced at least two orogenic events during the Mesozoic and Cenozoic. Early Mesozoic orogeny is characterized by intra-continental shortening in response to the amalgamation of the South China and Qiangtang continental blocks to North China (Chen et al., 1994; Yan et al., 2011; 2018). In the western Sichuan Basin

Mesozoic shortening is recorded by thrusts of strongly folded early Paleozoic strata over Triassic-Jurassic sediments (Fig. 2). This was accompanied by the development of a Mesozoic syn-deformation foreland basin (Sichuan Basin) (SBGMR, 1991; Li et al., 2003; Jia et al., 2006), and Mesozoic structures and metamorphic events along the LMSFZ (SBGMR, 1991; Burchfiel et al., 1995; Yan et al., 2011; 2018). Cenozoic deformation reactivated Mesozoic structures in response to continued indentation of India into Eurasia.

Structures along the LMSFZ are defined by three SW-striking sub-parallel faults, namely the Guanxian-Anxian, Yinxiu-Beichuan and Wenchuan-Maoxian faults, from east to west (Fig. 1). These faults dip steeply to the northwest, as shown by surface geological mapping (Fig. 2), deformation of Quaternary sediments (Densmore et al., 2007), deep seismic reflection profiles (Jia et al., 2006; Guo et al., 2013; Feng et al., 2016) and borehole data (Li et al., 2013). Further west, several more NE-NEE-striking faults developed in the hinterland area. These are the Qingchuan fault, Xueshan fault and East Kunlun faults (including the Tazang, Bailongjiang, Feng-Tai and Hanan branches). These faults link up with the N-striking and W-dipping Huya and Minjiang faults, that experienced >7 km of rock uplift during the late Cenozoic (Tian et al., 2018). It is worth noting that *Kirby et al*. (2000), noted the east end of the Xueshan fault was truncated by a Mesozoic granite (Fig. 2) and therefore initiation of the fault must pre date emplacement. Except for this fault, the other faults were all active during the late Cenozoic, as indicated by earthquake activities, offset landforms and exhumation data (e.g., Kirby et al., 2000; Ren et al., 2013; Tian et al., 2018).

Late Cenozoic deformation of the LMSFZ is of a listric thin-skinned style, based on three lines of evidence: First, listric geometries are shown by both surface geology and seismic reflection profiles in all segments of the LMSFZ (Jia et al., 2006; Feng et al., 2016). Second, inversion of fault slip using high-resolution geodetic data (GPS and InSAR) suggest most of the earthquake slip occurred on steeply dipping fault planes that root into a basal décollement (e.g., Wang et al., 2011). Third, enhanced late Miocene erosion in the southern and central segment of the LMSFZ shows a westward decreasing trend, consistent with the pattern of rock uplift over an upper crustal listric fault (Tian et al., 2013; Tan et al., 2017).

Late Cenozoic deformation in the northern LMSFZ, the study area, is dominated by transpression evidenced by seismic profile imaging that suggest underground structures of the region are characterized by a flower structure rooting into the Qingchuan fault and overprinting earlier deformation (Fig. 4a). Also, the surface rupture of the 2008 Wenchuan earthquake produced ca. 2 m coseismic slip in both vertical and horizontal directions (Liu-Zeng et al., 2009). Focal mechanisms of the aftershocks are mainly right-lateral strike-slip (Figs. 1b, 4b). Holocene right-lateral slip rates, estimated by offset terraces, range between 1-10 mm/yr (Densmore et al., 2007; Godard et al., 2010) but offset streasms record a slower rate over the longer term, ca. 1-2 mm/yr (Jia et al., 2010).

3. Previous thermochronological studies

Thermochronological studies in the eastern Tibetan Plateau have provided important constraints on the regions exhumation history and driving mechanisms. Reported data from the eastern Tibetan Plateau, compiled in figure 1, suggests a spatially variable exhumation pattern. In the southern and central segments of the LMSFZ, 2-5 km of episodic rock exhumation occurred during the Oligocene – early Miocene and late Miocene (Wang et al., 2012). However, in the Min Shan, > 7 km of exhumation occurred during the late Miocene, preceded (Oligocene – early Miocene) by minor (<1 km) exhumation (Tian et al., 2018). Similar to the Min Shan, the evolution of the plateau interior is characterized by slow pre-late Miocene exhumation, followed by enhanced rates (ca. 0.3-0.5 km/myr) since ca. 10 Ma (Arne et al., 1997; Kirby et al., 2002; Clark et al., 2005b; Ouimet et al., 2010; Roger et al.,2011; Tian et al., 2015; Ansberque et al., 2018). In the Sichuan Basin, thermal history models suggest slow exhumation before ca. 30-45 Ma, after which rates increased (Richardson et al., 2008; Tian et al., 2012). Comparatively few apatite fission-track ages have been reported for the northern segment of LMSFZ. These range from 30-70 Ma (Arne et al., 1997; Enkelmann et al., 2006; Yan et al., 2011; Li et al., 2012), and are significantly older than regions to the south, which suggest that the northern segment experienced a different exhumation history from other segments.

4. Sampling, experimental methods

4.1. Sampling and analytical strategies

We applied multi-thermochronology methods, including apatite U-Th-He (AHe), zircon U-Th-He (ZHe) and apatite fission-track (AFT) analyses along a ca. 150-km-long surface transect in the northern segment of the LMSFZ, comprising four granites, seven sandstones and one meta-sandstone (Table 1, Figs. 2-3). AFT ages of five of the samples (HS15-19) were reported by Tian et al. (2018), which focused on the late Cenozoic rock exhumation and deformation of the adjacent Min Shan region. For this study we produced a more detailed reconstruction of the thermal and tectonic evolution, across a larger area. We built on the dataset of Tian et al. (2018) with new AFT length measurements, AHe and ZHe ages on samples HS15-19 as well as producing new data for seven new samples collected from a transect that spans the major faults in the northern LMSFZ, namely the Qingchaun fault, Yingxiu-Beichuan fault, and Guanxian-Anxian fault, from west to east (Fig. 3). The dataset comprises eight samples (HS12-HS19) from the west side of the Yingxiu-Beichuan fault, ruptured by the 2008 Wenchuan Earthquake, and a further four samples (HS2, HS4, HS7 and HS11) from the east side.

4.2. Analytical Methods

Apatite and zircon concentrates were obtained by standard crushing, sieving, electromagnetic and heavy liquid mineral separation techniques.. Apatites were mounted in epoxy resin on glass slides, ground, and polished to an optical finish to expose internal grain surfaces. Mounts were etched in 5-M HNO_3 for 20 s at 21 °C to reveal fossil tracks. An aluminum coating (ca. 5–7 nm thickness) was applied to the etched mounts using a vacuum coating unit so as to enhance the reflectivity of the polished surface and minimize internal reflections under the microscope (Gleadow et al., 2009). Apatite grains with polished surfaces parallel to prismatic crystal faces and homogeneous track distributions were selected using a Zeiss Axio Imager M1m microscope. Then stacks of high-resolution digital images of each selected grain were taken at a total magnification of 1000x under both transmitted and reflected light using a Zeiss camera. The pixel size (ca. 0.0698–0.0705 μm/pixel) of the images was precisely calibrated. Track counting was performed using the coincidence mapping protocol and then verified and corrected manually (Gleadow et al., 2009). Uranium measurements of selected grains were carried out on an Agilent 7700 ICP-MS using a pulsed (Q-switched) Nd:YAG (neodymium-doped yttrium aluminum garnet) laser with a wavelength of 213 nm. Laser ablation under consistent laser conditions (25-μm diameter beam size, ca. 2.5-J/cm_2 energy, and 10-Hz repetition rate) was applied to selected grains and NIST-612 (uranium standard) for 25 s. NIST-612 glass $^{238}U/^{43}Ca$ ratio and apatite ^{43}Ca were used as internal standards to correct for drift in instrument sensitivity and variations in ablation volume between dated grains, respectively. Etch pit diameters (Dpar) of grains were also determined on tracks used for density and length measurements. Detailed results are provided in Table 1.

For (U-Th)/He analysis, grains were immersed in ethanol and examined under polarized light to detect possible mineral inclusions and digitized photographs were taken for the calculation of an α-ejection correction factor (Ft) (Ketcham et al., 2011). Only good-quality euhedral grains, where possible, were selected for analysis. Grains were loaded into Pt capsules and thermally outgassed under vacuum at ca. 900 °C for 5 min for apatite and ca. 1,300 °C for 15 min for zircon, using a fiber optically coupled diode laser with 820 nm wavelength. A spike of ^{3}He was used to determine gas volumes measured using a Balzers quadrupole mass spectrometer. The uncertainty in the sample ^{4}He measurement is estimated at <1%. Outgassed apatite grains were then spiked and digested in nitric acid at room temperature. For zircon analyses, outgassed grains were first taken out of their Pt capsules and transferred to Parr bombs where they were spiked with ^{235}U and ^{230}Th and digested at 240 °C for 40 hr in HF. Standard solutions containing the same spike amounts as samples were treated identically, as were a series of unspiked reagent blanks. A second bombing in HCl for 24 hr at 200 °C ensured dissolution of fluoride salts and final solutions were diluted to 10% acidity for analysis on a Varian quadrupole ICP-MS. For single zircon crystals digested in small volumes

(0.3–0.5 ml), U and Th isotope ratios were measured to a precision of <2%. Unless otherwise indicated, apparent ZHe ages were calculated and corrected for α emission following the approach of Farley et al. (1996). Durango apatite and Fish Canyon Tuff zircons were run as standards with each batch of samples analyzed and served as an additional check on analytical accuracy. Based on the standards, we estimated a precision of ca. 6% or less at ± 1σ, which incorporates the α correction-related constituent and considers an estimated 5-μm uncertainty in grain size measurements, gas analysis, and ICP-MS uncertainties. The detailed results are tabulated in Table 2.

4.3. Inverse thermal history modeling

Inverse thermal history modeling of individual and joint samples used the Bayesian transdimensional Markov Chain Monte Carlo protocol of Gallagher (2012, QTQt program version 5.7.0). The multi-kinetic annealing model of Ketcham et al. (2007) was used for modeling AFT data, using projected lengths and Dpar values as kinetic parameters. Helium diffusion in apatite and zircon applied the radiation damage accumulation and annealing models of Flowers et al. (2009) and Guenthner et al. (2013), respectively. For detailed information concerning the sequence of steps and parameter settings, see Gallagher (2012). The modeling was applied to samples with multiple ZHe, AFT and AHe ages, and sufficient AFT lengths (>75). Samples with limited data (HS13, HS15 and HS18) were not modeled because the temperature history solution for such samples without multiple thermochronological data is non-unique.

Reasonable geological constraints can eliminate geologically unreasonable thermal paths, and make inverse modeling results more informative. However, too many constraints may artificially drive the modeling results (Vermeesch and Tian, 2014). Prior geological constraints include the following: (1) present-day temperature for surface samples (15 ± 15 ℃); (2) default time-temperature space, 100 ℃ (± 100% variation, if inputs include ZHe data) or 70 ℃ (± 100% variation, if inputs are AFT and AHe data) during the time of the oldest age ± 100% variation. (3) For Jurassic-Cretaceous sandstone samples (HS2, HS4 and HS7), a temperature constraint of 20 ± 20 ℃ was applied to the depositional age.

For modeling sample groups east of the Yingxiu-Beichuan fault, prior geological constraints include a present-day temperature for surface samples of 15 ± 15 °C, a geothermal gradient 20 ± 15 °C/km, similar to the present-day gradient of ~20 °C/km (Xu et al., 2011), and an early Cretaceous constraint (120 ± 20 Ma) at 20 ± 20 °C to reflect deposition of the early Cretaceous samples. The broad temperature and time range give the modeling sufficient freedom to search for data-constrained thermal histories based on one million iterations to derive stable inverse model results.

5. Structural, thermochronological and thermal history modeling results

5.1. Structural observations

Our field observations along the Yingxiu-Beichuan fault zone in the northern segment of the LMSFZ show that folded early Paleozoic strata were cut by brittle faults (Fig. 5). Shear senses were determined from brittle kinematic indicators including steps and fractures (Fig. 5b-c). A stereonet plot of all field measurements of fault planes and striations suggests the fault zone consists of brittle NNE-NE-trending right-lateral, ESE-trending left-lateral and SE-trending tensional micro-faults (Fig. 5e, Supplementary Data TS1). The combination of micro-faults with different slip senses can be explained by the classical Riedel shears along a NE-striking main right-lateral shear zone (Fig. 5f, Tchalenko, 1970). In the study area, right-lateral strike-slip faults (red in Fig. 5e) correspond to the R and P structures, left-lateral ones are R' shears (blue in Fig. 5e), whereas those extensional fractures (magenta in Fig. 5e) are tensional joints.

5.2. Thermochronology results

In total, we present twelve AFT ages, forty-six single-grain AHe ages from seven samples and twelve single-grain ZHe ages from three samples (Fig. 3). To facilitate comparison, these data are projected onto the AA' swath (Fig. 6).

AFT data

AFT ages exhibit diachroneity between the east and west sides of the Yingxiu-

Beichuan fault. Eight samples (HS12-HS19) from the west side of the fault produce AFT ages ranging between 40.8 ± 4.1 and 72.8 ± 5.8 Ma; whereas three samples (HS2, HS4, HS7, HS11) from the east side are significantly older, between 86.4 ± 6.6 and 103.7 ± 4.8 Ma. AFT ages from Jurassic - Cretaceous sandstone samples (HS2, HS4 and HS7), from the east side, are slightly younger than their depositional ages, indicating that they are partially reset. Data from pre-Mesozoic sandstone and Mesozoic granite samples from the west side, including HS11, are younger than their deposition or formation ages and are thus fully reset (Table 1). These differences are also reflected by differences in sample elevations. Older sample ages on the east side of the fault come from lower elevations (500-600 m) compared to the west side (650-1700 m) where ages are younger (Fig. 7a and Table 2). This pattern reflects differential exhumation across the fault.

Mean track lengths (MTL) from the west side of the Yingxiu-Beichuan fault are consistent, ranging between 12.9 ± 0.2 μm and 13.7 ± 0.1 μm; whereas those from the east side are relatively shorter varying from 11.9 ± 0.1 μm to 12.9 ± 0.2 μm (Fig. 6, Table 2). The slightly shorter MTL and wider track length distribution (as shown by greater relative standard deviations) of samples from the east side indicate a longer period of residence in the AFT partial annealing zone (60-120℃) than western samples. Dpar values are similar, between 1.4-2.0 μm, ruling out major compositional differences as an explanation for the age differences seen on either side of the fault.

AHe and ZHe data

AHe ages also show differences between the two sides of the Yingxiu-Beichuan fault. AHe ages of five sandstone and granite samples (HS12, HS14, HS16, HS17, HS19) from the west side of the fault yield latest Cretaceous - early Oligocene single-grain ages; and their weighted means calculated using IsoplotR (Vermeesch, 2018) are 50 ± 4.1, 62.5 ± 2.7, 43.9 ± 3.6, 57.2 ± 2.3 and 44.8 ± 3.0 Ma, respectively (Table 2, Fig. 6). Single-grain AHe ages of two samples (HS4 and HS7) from the east side of the fault are mostly Eocene – Miocene with a couple of late Cretaceous – Paleocene outliers. Their weighted means are 43.6 ± 1.8 and 34.5 ± 2.0 Ma, respectively (Table 2, Fig. 6), slightly younger than those from the west side. All ZHe data come from the west side of the Yingxiu-Beichuan fault. ZHe analyses of three granite samples (HS14, HS16 and HS19) yield early – late Cretaceous single-grain ages, with weighted mean ages of 104.6 ± 3.6, 100.8 ± 4.3, 116.4 ± 4.7 Ma, respectively (Table 2, Fig. 6).

5.3. Thermal modelling results and interpretations

A plot of ages for different thermochronometers versus their closure temperatures shows an early Cretaceous - Eocene phase of enhanced cooling for samples from the west side of the Yingxiu-Beichuan fault (Fig. 7b). To further test this observation thermal history models were produced for each sample. Thermal history modeling for five samples from the west side of the Yingxiu-Beichuan fault shows relatively rapid late Cretaceous-Eocene cooling at a rate of ~3-5 ^{o}C/Myr, followed by slow cooling (<0.5 ^{o}C/Myr) to the present day (Fig. 8). This first-order cooling pattern is consistent with the age – closure temperature plot (Fig. 7b). Detailed thermal histories of these samples vary slightly in terms of the cooling rates and the end time of the late Cretaceous-Eocene phase of cooling. For example, the cooling in samples HS12, HS17, HS19 occurred at relatively higher rates than other samples (HS14 and HS16). Exhumation of sample HS19 took place at about 30 Ma which is slightly later than the other samples (45-40 Ma). These second-order cooling features probably indicate differential vertical displacements. Further, for samples HS14, HS16 and HS19, that have additional ZHe data, modelling results suggest a phase of slow cooling before the late Cretaceous (Fig. 8b, 8c and 8e).

Modeling for the four samples (HS2, HS4, HS7 and HS11) from the other side of the Yingxiu-Beichuan fault yielded a contrasting thermal history characterized by poorly resolved pre-Eocene cooling/heating, followed by accelerated rates of cooling commencing at ca. 40-60 Ma (Figs. 9a-c). Given the high levels of similarity in both the fission-track data and thermal history inversion results, we performed joint modeling to further refine their temperature histories. The results reveal episodic early Cretaceous reheating, presumably due to sediment burial, followed by cooling since

~40-50 Ma.

To summarize, our low-temperature thermochronology data and temperature history inversions show a contrast in post late Cretaceous cooling histories between the hinterland (west of the marginal Yingxiu-Beichuan fault) and the foreland (east of the fault). As late Cretaceous – Cenozoic magmatism activity is absent from the northern segment of the LMSFZ (Fig. 2 and SBGMR, 1991), the cooling histories inferred from our data reflect coeval rock exhumation. Before the Eocene (ca. 40 Ma) the hinterland underwent significant cooling and exhumation but the foreland only experienced minor exhumation. However, after the Eocene, there was a reversal such that only minor exhumation occurred in the hinterland whereas the foreland side experienced accelerated exhumation. This variable exhumation reflects differential rock uplift across the Yingxiu-Beichuan fault.

6. Discussion

6.1. Pre-Cenozoic exhumation in the LMSFZ

Development of topographic relief in the LMSFZ has been previously regarded as resulting from late Cenozoic deformation (Kirby et al., 2002; Godard et al., 2009; Tian et al., 2013; Tan et al., 2019). However, our results show enhanced rock cooling and exhumation in the northern LMSFZ mainly occurred during late Cretaceous-Eocene and therefore provides new insight into the pre-Cenozoic ~~topographic growth, as surface erosion is a non-linear positive function of topographic relief and precipitation (e.g., Montgomery and Brandon, 2002).~~ Given that the Asia paleoclimate was relatively constant and mainly arid during the late Cretaceous to Eocene (Guo et al., 2008; Wang et al., 2013; Farnsworth et al., 2019), the likelihood of a climatic origin for the enhanced cooling and exhumation in the hinterland can be ruled out. An alternative possibility is that the enhanced cooling in the late Cretaceous-Eocene is related to erosional topographic decay of the LMSFZ, due to unloading. This scenario would produce a coeval isostatic rebound and erosion of the foreland basin, inconsistent with the preserved basin strata. The youngest strata in the adjacent foreland side are lower Cretaceous, but there must have been younger overlying deposits, as the lower

Cretaceous strata are heavily lithified, and thermal history models indicate an interval of reheating likely due to burial (Fig. 9). It is therefore considered that this pulse of accelerated cooling and exhumation has a tectonic origin and records the fluvial response to enhanced rock uplift.

Recent structural observations in the southern segment of the LMSFZ show late Cretaceous – Paleogene upper crustal duplexing, foreland basin development and associated growth strata in the foreland (Tian et al., 2016). The late Cretaceous-Eocene phase of rock exhumation has not been identified in previous low-temperature thermochronology studies in the southern and central segments of the LMSFZ, probably because thermochronological fingerprints of the early exhumation have been removed by more intensive and deeper (>7 km) late Cenozoic exhumation therein (Godard et al., 2009; Wang et al., 2012; Cook et al., 2013; Tian et al., 2013; Tan et al., 2019). This phase of shortening is likely to be a far-field effect of the closure of the Neo-Tethys ocean and early Cenozoic continental collision between India and Eurasia, as inferred for regions further to the north (e.g., Ratschbacher et al., 2003; Hu et al., 2006).

6.2. Tectonic transition in the northern LMSFZ

Geological and seismic evidence suggest the initiation of right-lateral slip in the northern LMSFZ occurred before at least the late Cenozoic (Figs. 4 and 5), as outlined above. Considering the presence of late Cretaceous shortening, the northern LMSFZ should have experienced a Cenozoic transition phase from shortening to right-lateral slip, which would have overprinted earlier deformation features (Figs. 4 and 5). We propose that this transition occurred during the Eocene, as evidenced by post Eocene differential exhumation between the hinterland and the foreland (Fig. 10). On the one hand, given that we observed low rates of post Eocene exhumation in the hinterland areas, it is likely that the area experienced tectonic quiescence or local strike-slip deformation without significant vertical uplift since the Eocene (ca. 40 Ma). On the other hand, enhanced post Eocene cooling and exhumation in the western part of the Sichuan Basin (east of the Yingxiu-Beichuan fault) requires a mechanism for explaining associated rock uplift. The proposed Eocene tectonic transition from shortening to right-lateral slip predicts a decrease in the tectonic and topographic loading over the western margin of the Sichuan Basin and this would induce crustal isostatic rebound characterized by low heat flow, high strength and elasticity (Wang et al., 2010; Xu et al., 2011; Chen et al., 2013), which would explain post-Eocene exhumation in the western Sichuan Basin (Fig. 10).

Our proposal is consistent with magnetostratigraphic and structural studies in the Hui-Cheng Basin (~100 km north of the study area), bounded by the Feng-Tai, Mianlue and Hanan faults (Fig. 1b), which suggest a Paleogene tectonic transition from NNW-SSE shortening to strike-slip displacement along E- and NE-trending faults (Li et al., 2019; Hu et al., 2020). As discussed below (section 6.3), the eastern Tibetan Plateau has also experienced a late Miocene phase of tectonic adjustment, characterized by the formation of the Huya and Minjiang faults (Tian et al., 2018) and enhanced exhumation in both southern-central LMSFZ and areas to the west. Such an adjustment may imply the possibility of late Miocene initiation of strike-slip deformation in the northern LMSFZ. However, the late Miocene timing is inconsistent with the Paleogene switch from shortening to strike-slip deformation, seen in the Hui-Cheng Basin. In addition, no enhanced late Miocene exhumation was detected in our samples from the northern LMSFZ. Future studies can test for this using direct dating of syn-deformation carbonate veins and slickenside deposits (such as those shown in Figs. 5a-c) (e.g., Roberts and Holdsworth, 2022 and references therein).

6.3. Strain migration in the eastern Tibetan Plateau

Over the broader eastern margin, Cretaceous – Cenozoic deformation has been accommodated by different structures in different ways and at different times. These structures include the LMSFZ, Huya, Minjiang, Tazang, Bailongjiang, Feng-Tai and Hanan faults. During the late Cretaceous – early Cenozoic, crustal shortening in the eastern margin of the Tibetan Plateau has been mapped on the NE-trending LMSFZ, the Feng-Tai and Hanan faults. On the LMSFZ, shortening has been documented by the following lines of evidence: (1) Upper crustal thrust duplexing in the southern and central segment of the LMSFZ, as shown by structural and magnetic fabric studies (Tian et al., 2016; Xue et al., 2017; Airaghi et al., 2018) that Ar-Ar data record as late Cretaceous-earliest Paleocene (Tian et al., 2016; Airaghi et al., 2018). (2) Formation of a coeval foreland basin (with ca. 1.5 km of non-marine sediments) in the southwest corner of the Sichuan Basin (Jia et al., 2006; Tian et al., 2016). (3) Accelerated late Cretaceous – Eocene exhumation in the hinterland of the northern LMSFZ that support late Cretaceous – early Cenozoic shortening, as discussed above. On the Feng-Tai and Hanan faults, late Cretaceous shortening was mainly documented by the folding of Cretaceous deposits (paleomagnetically dated) in the Hui-Cheng Basin by NNW-SSE shortening (Li et al., 2019; Hu et al., 2020). The development of these NE-trending reverse faults and folds indicates a regional NW-SE contractional stress-field (Fig. 11a).

The Eocene tectonic transition from shortening to strike-slip faulting occurred on both the northern segment of LMSFZ (as discussed above) and the Feng-Tai and Hanan faults (Fig. 11b). Late Cretaceous shortening of the Hui-Cheng Basin was overprinted by strike-slip displacement along NE-trending faults, whose age was inferred as the Paleogene (Li et al., 2019). These structures suggest a SW-NE contractional stress regime oblique to the LMSFZ.

In the southern segment, shortening lasted from late Cretaceous to the entire Cenozoic, supported by the following lines of evidence: Foredeep deposits extended to the Oligocene (SBGMR, 1991; Burchfiel et al., 1995). Post-Eocene shortening must have occurred within the southwestern part of the Sichuan Basin, recorded by a thrust underpinning the Xiongpo thrust-related anticline whose ages are constrained as the Eocene by enhanced cooling and exhumation in the hanging wall (Richardson et al., 2008). Miocene shortening has alsdo been documented by differential exhumation across faults in the southern and central LMSFZ (Cook et al., 2013; Tian et al., 2013; Tan et al., 2017).

The late Miocene also witnessed a major tectonic change linked to initiation of the south-striking Huya and Minjiang faults (Fig. 11c). Recent thermochronology studies revealed late Cenozoic (ca. 10 Ma) differential rock exhumation across those two faults, with a higher exhumation rate (ca. 0.7 km/m.y.) in the hanging wall, which has been interpreted as resulting from NE-ward upper crustal thrusting (Tian et al., 2018). This phase of shortening also occurred on nearby faults along the southern and central LMSFZ, as outlined above.

Modern active deformation in the eastern margin of the Tibetan Plateau follows the late Cenozoic structures (Fig. 11c). We note three lines of evidence: First, active deformation, shown by earthquake focal mechanisms, transformed from reverse, via oblique, to strike-slip from the southern to northern LMSFZ, similar to post-Eocene along-strike variable deformation along the fault zone. Second, several large historic earthquakes (M. > 6.5), with strike-slip and reverse focal mechanisms, occurred on the Huya and Minjiang faults. Third, the Tazang, Bailongjiang, Hanan and Feng-Tai faults have also been actively deformed by left-lateral slip, as shown by recent large earthquakes (Fig. 11c) and displaced landforms (Ren et al., 2013; Liu et al., 2012; Liu et al., 2015; Li et al., 2020). Displaced geomorphic features, dated by radiocarbon and optically stimulated luminescence methods, indicate a millennial slip rate of 1.4–3.2 mm/yr and 1.5-0.2 mm/yr along its western and easternmost parts of the Tazang Fault, respectively (Ren et al., 2013). It is worth noting that late Cenozoic south-verging thrusts have been mapped along the surface outcrop of the Hanan fault, including thrusts developed on Pleistocene loess (Li et al., 2020). These indicate the Hanan fault is probably an oblique left-lateral fault.

6.4. Implications for plateau growth mechanisms

These new results have important implications for the growth of the Tibetan Plateau. One group of models highlight lithospheric scale shortening and lateral extrusion of coherent crustal blocks along major pre-existing mechanically weak belts (Tapponnier et al., 2001; Jiang et al., 2019). Our results do not fit the lithospheric extrusion model for Plateau growth, as do numerous other studies that indicate deformation in the LMSFZ is of a thin-skinned style (Jia et al., 2006; Tian et al., 2013; Feng et al., 2016). Likewise, the extrusion model predicts Oligo-Miocene shortening in the LMSFZ (Tapponnier et al., 2001), which cannot explain the observed Eocene transition of deformation.

A second group of models infers that uplift of the Tibetan Plateau resulted from lower crustal thickening, which has been redistributed by gravitation-driven ductile flow away from the plateau interior to the margins (Royden et al., 2008). This model is consistent with geophysical observations, such as negative seismic velocity anomalies and high electrical conductivity in the middle-lower crustal (Xu et al., 2007; Bai et al., 2010). But this ‘channel flow’ model predicts late Miocene deformation across the plateau margins after crustal thickening in the southern and central plateau, which is inconsistent with our Eocene observations.

Finally, pure-shear shortening in the lower crust may have occurred (Yin, 2010; Tan et al., 2019). However, as indicated by the pattern of exhumation recorded by thermochronology data, deformation along the eastern margin of the Tibetan Plateau is of a short wave-length and controlled mostly by upper crustal structures (Tian et al., 2013, 2018; Tan et al., 2019; and this work). Therefore, shortening in the lower crust or lithosphere should be minor, as it predicts long-wavelength crustal deformation and exhumation.

An increasing number of studies, including this one, reported early Cenozoic deformation along the current plateau margins. For example, structural, geochronological and thermochronological studies indicate early Cenozoic shear in the Qinling-Dabie orogen (Ratschbacher et al., 2003; Hu et al., 2006), exhumation and reverse faulting in the Qilian Shan and Qinling (Clark et al., 2010; Duvall et al., 2011; Wang et al., 2017; Zhuang et al., 2018; Zhang et al., 2020; Wang et al., 2022), upper crustal shortening and duplexing in the southern segment of the LMSFZ (Tian et al., 2016), rock exhumation in the southeastern Tibetan Plateau (Liu-Zeng et al., 2018), transpressional deformation in the Altyn Tagh Fault (northern Tibetan Plateau) (Wu et al., 2019). Together, these studies support rapid strain transfer from the collision zone towards regions that now form the plateau margins, and this draws attention to the role of early Cenozoic deformation in plateau formation.

CONCLUSIONS

Our new low-temperature thermochronology results from the northern segment of the LMSFZ identified a late Cretaceous – Eocene phase of cooling and exhumation followed by low rates of exhumation in the hinterland, west of the Yingxiu-Beichuan Fault. This contrasts with the foreland side of the mountain range, which is characterized by a significant acceleration in post-Eocene exhumation. These results support a major tectonic change from a shortening-dominated to strike-slip-dominated regime in the middle Eocene. Before ca. 40 Ma, the deformation in the northern segment of the LMSFZ was characterized by upper crustal shortening. The Eocene transition into a strike-slip regime predicts a decrease in the tectonic and topographic loading over the western margin of the foreland Sichuan Basin, causing the observed post-Eocene cooling and exhumation in the western part of the basin.

A compilation of fault deformation history for the eastern Tibetan Plateau suggests that the Eocene tectonic transition from shortening to strike-slip faulting occurred on other NE-trending faults (such as the Feng-Tai and Hanan faults). Our compilation also shows a late Cenozoic tectonic transition, characterized by the formation of the south-striking Huya and Minjiang faults in the late Miocene. Finally, our results highlight the importance of progressive late Eocene and late Miocene tectonic transitions in shaping the eastern margin of the Tibetan Plateau.

Acknowledgments

Funding for this research was provided National Natural Science Foundation of China (NSFC) grant no. 42172229, 41888101 and 41772211. Suggestions from Profs. C. Deng and W. Wang and constructive comments from H. Zhang and an anonymous reviewer are gratefully acknowledged.

Reference

Airaghi, L., Warren, C. J., de Sigoyer, J., Lanari, P., and Magnin, V., 2018, Influence of dissolution/reprecipitation reactions on metamorphic greenschist to amphibolite facies mica 40Ar/39Ar ages in the Longmen Shan (eastern Tibet): Journal of Metamorphic Geology 36 (7), 933-958.

Ansberque, C., Godard, V., Olivetti, V., Bellier, O., De Sigoyer, J., Bernet, M., Stübner,

K., Tan, X., Xu, X., and Ehlers, T. A., 2018, Differential exhumation across the Longriba fault system: Implications for the eastern Tibetan Plateau: Tectonics 37 (2), 663-679.
Arne, D., Worley, B., Wilson, C., She, F. C., Foster, D., Zhi, L. L., Shu, G. L., and Dirks, P., 1997, Differential exhumation in response to episodic thrusting along the eastern margin of the Tibetan Plateau: Tectonophysics 280 (3–4), 239-256.
Bai, D., Unsworth, M. J., Meju, M. A., Ma, X., Teng, J., Kong, X., Sun, Y., Sun, J., Wang, L., Jiang, C., Zhao, C., Xiao, P., and Liu, M., 2010, Crustal deformation of the eastern Tibetan plateau revealed by magnetotelluric imaging: Nature Geoscience 3 (5), 358-362.
Burchfiel, B. C., Zhiliang, C., Yupinc, L., and Royden, L. H., 1995, Tectonics of the Longmen Shan and Adjacent Regions, Central China: International Geology Review 37 (8), 661-735.
Chang, C., Chen, N., Coward, M.P., Deng, W., Dewey, J.F., Gansser, A., Harris, N.B.W., Jin, C., Kidd, W.S.F., Leeder, M.R., Li, H., Lin, J., Liu, C., Mei, H., Molnar, P., Pan, Y., Pan, Y., Pearce, J.A., Shackleton, R.M., Smith, A.B., Sun, Y., Ward, M., Watts, D.R., Xu, J., Xu, R., Yin, J. and Zhang, Y., 1986. Preliminary conclusions of the Royal Society and Academia Sinica 1985 geotraverse of Tibet. Nature, 323(6088), 501-507
Chen, B., Chen, C., Kaban, M.K., Du, J., Liang, Q., Thomas, M., 2013. Variations of the effective elastic thickness over China and surroundings and their relation to the lithosphere dynamics. Earth Planet. Sci. Lett. 363, 61-72.
Chen, S. F., and Wilson, C. J., 1996, Emplacement of the Longmen Shan Thrust—Nappe Belt along the eastern margin of the Tibetan Plateau: Journal of Structural Geology 18 (4), 413-430.
Chen, S. F., Wilson, C., Luo, Z. L., and Deng, Q. D., 1994, The evolution of the western Sichuan foreland basin, southwestern China: Journal of Southeast Asian Earth Sciences 10 (3-4), 159-168.
Clark, M. K., Bush, J. W., and Royden, L. H., 2005a, Dynamic topography produced by lower crustal flow against rheological strength heterogeneities bordering the Tibetan Plateau: Geophysical Journal International 162 (2), 575-590.
Clark, M. K., House, M. A., Royden, L. H., Whipple, K. X., Burchfiel, B. C., Zhang, X., and Tang, W., 2005b, Late Cenozoic uplift of southeastern Tibet: Geology 33 (6), 525-528.
Cook, K. L., Royden, L. H., Burchfiel, B. C., Lee, Y. H., and Tan, X., 2013, Constraints on Cenozoic tectonics in the southwestern Longmen Shan from low-temperature thermochronology: Lithosphere 5 (4), 393-406.
Deng, B., Liu, S.-g., Enkelmann, E., Li, Z.-w., Ehlers, T. A., and Jansa, L., 2015, Late Miocene accelerated exhumation of the Daliang Mountains, southeastern margin of the Tibetan Plateau: International Journal of Earth Sciences 104 (4), 1061-1081.
Densmore, A. L., Ellis, M. A., Li, Y., Zhou, R., Hancock, G. S., and Richardson, N., 2007, Active tectonics of the Beichuan and Pengguan faults at the eastern margin of the Tibetan Plateau: Tectonics 26, doi:10.1029/2006TC001987.

Duvall, A. R., Clark, M. K., van der Pluijm, B. A., and Li, C., 2011, Direct dating of Eocene reverse faulting in northeastern Tibet using Ar-dating of fault clays and low-temperature thermochronometry: Earth Planetary Science Letters 304 (3-4), 520-526.

Enkelmann, E., Ratschbacher, L., Jonckheere, R., Nestler, R., Fleischer, M., Gloaguen, R., Hacker, B. R., Zhang, Y. Q., and Ma, Y. S., 2006, Cenozoic exhumation and deformation of northeastern Tibet and the Qinling: Is Tibetan lower crustal flow diverging around the Sichuan Basin?: Geological Society of America Bulletin 118 (5-6), 651-671.

Fan, C., Wang, E., Wang, S., and Wang, G., 2008, Dextral strike-slip and tectonic transformation of the northern segment of Longmen Shan fault belt from Late Neogene: A case study from the Qingchuan fault: Chinese Journal of Geology 3.

Farnsworth, A., Lunt, D., Robinson, S., Valdes, P., Roberts, W., Clift, P., Markwick, P., Su, T., Wrobel, N., Bragg, F., Kelland, S.-J., Pancost, R., 2019. Past East Asian monsoon evolution controlled by paleogeography, not CO2. Science Advances 5, doi: 10.1126/sciadv.aax1697

Feng, S. y., Zhang, P. z., Liu, B. j., Wang, M., Zhu, S. b., Ran, Y. k., Wang, W. t., Zhang, Z. q., Zheng, W. j., and Zheng, D. w., 2016, Deep crustal deformation of the Longmen Shan, eastern margin of the Tibetan Plateau, from seismic reflection and Finite Element modeling: Journal of Geophysical Research: Solid Earth 121 (2), 767-787.

Flowers, R. M., Ketcham, R. A., Shuster, D. L., and Farley, K. A., 2009, Apatite (U–Th)/He thermochronometry using a radiation damage accumulation and annealing model: Geochimica Et Cosmochimica Acta 73 (8), 2347-2365.

Gallagher, K., 2012, Transdimensional inverse thermal history modeling for quantitative thermochronology: Journal of Geophysical Research: Solid Earth 117, doi:10.1029/2011JB008825.

Gleadow, A. J. W., Gleadow, S. J., Belton, D. X., Kohn, B. P., Krochmal, M. S., and Brown, R. W., 2009, Coincidence mapping - A key strategy for the automatic counting of fission tracks in natural minerals: Geological Society London Special Publications 324 (1), 25-36.

Godard, V., Pik, R., Lavé, J., Cattin, R., Tibari, B., de Sigoyer, J., Pubellier, M., and Zhu, J., 2009, Late Cenozoic evolution of the central Longmen Shan, eastern Tibet: Insight from (U-Th)/He thermochronometry: Tectonics 28, doi:10.1029/2008TC002407.

Godard, V., Lavé, J., Carcaillet, J., Cattin, R., Bourlès, D., and Zhu, J., 2010, Spatial distribution of denudation in Eastern Tibet and regressive erosion of plateau margins: Tectonophysics 491 (1-4), 253-274.

Guenthner, W. R., Reiners), W., Ketcham, R. A., Nasdala, L., and Giester, G., 2013, Helium diffusion in natural zircon: Radiation damage, anisotropy, and the interpretation of zircon (U-Th)/He thermochronology: American Journal of Science 313 (3), 145-198.

Guo, X., Gao, R., Randy Keller, G., Xu, X., Wang, H., and Li, W., 2013, Imaging the

crustal structure beneath the eastern Tibetan Plateau and implications for the uplift of the Longmen Shan range: Earth and Planetary Science Letters 379, 72-80.
Guo, Z.T., Sun, B., Zhang, Z.S., Peng, S.Z., Xiao, G.Q., Ge, J.Y., Hao, Q.Z., Qiao, Y.S., Liang, M.Y., Liu, J.F., Yin, Q.Z. and Wei, J.J., 2008. A major reorganization of Asian climate regime by the early Miocene. Climate of the Past, 4(3): 535-584.
Hu, S., Raza, A., Min, K., Kohn, B. P., Reiners, P. W., Ketcham, R. A., Wang, J., and Gleadow, A. J., 2006, Late Mesozoic and Cenozoic thermotectonic evolution along a transect from the north China craton through the Qinling orogen into the Yangtze craton, central China: Tectonics 25, doi:10.1029/2006TC001985.
Hu, X., Zhang, Y., Li, Y., Ma, S., Li, J., 2020. Post-orogenic tectonic evolution of the Qinling belt, central China: Insights from a magnetostratigraphic study of a Cretaceous intra-mountain basin sedimentary succession. J. Asian Earth Sci. 202, https://doi.org/10.1016/j.jseaes.2020.104496
Hubbard, J., and Shaw, J. H., 2009, Uplift of the Longmen Shan and Tibetan plateau, and the 2008 Wenchuan (M = 7.9) earthquake: Nature 458 (7235), 194-197.
Jia, Y. Y., Fu, B. H., Wang, Y., Shi, P., and Liu, F., 2010, Late Cenozoic tectono-geomorphic growth and drainage response in the Longmen Shan fault zone, east margin of Tibet: Quaternary Sciences 30 (4), 825-836.
Jia, D., Wei, G., Chen, Z., Li, B., Zeng, Q., and Yang, G., 2006, Longmen Shan fold-thrust belt and its relation to the western Sichuan Basin in central China: New insights from hydrocarbon exploration: AAPG Bulletin 90 (9), 1425-1447.
Jiang, X., Li, Z.-X., Li, C., and Gong, W., 2019, A Gravity Study of the Longmenshan Fault Zone: New Insights Into the Nature and Evolution of the Fault Zone and Extrusion-Style Growth of the Tibetan Plateau Since 40 Ma: Tectonics 38 (1), 176-189.
Ketcham, R. A., Carter, A. C., Donelick, R. A., Barbarand, J., and Hurford, A. J., 2007, Improved modeling of fission-track annealing in apatite: American Mineralogist 92 (5-6), 799-810.
Ketcham, R. A., Gautheron, C., and Tassan-Got, L., 2011, Accounting for long alpha-particle stopping distances in (U–Th–Sm)/He geochronology: Refinement of the baseline case: Geochimica Et Cosmochimica Acta 75 (24), 7779-7791.
Kirby, E., Reiners, P. , W., Krol, M. A., Whipple, K. X., Hodges, K. V., Farley, K. A., Tang, W., and Chen, Z., 2002, Late Cenozoic evolution of the eastern margin of the Tibetan Plateau: Inferences from40Ar/39Ar and (U-Th)/He thermochronology: Tectonics 21 (1), 1-1-1-20.
Kirby, E., Whipple, K. X., Burchfiel, B. C., Tang, W., Berger, G., Sun, Z., and Chen, Z., 2000, Neotectonics of the Min Shan, China: Implications for mechanisms driving Quaternary deformation along the eastern margin of the Tibetan Plateau: Geological Society of America Bulletin 112 (3), 375-393.
Li, H., Wang, H., Xu, Z., Si, J., Pei, J., Li, T., Huang, Y., Song, S.-R., Kuo, L.-W., Sun, Z., Chevalier, M.-L., and Liu, D., 2013, Characteristics of the fault-related rocks, fault zones and the principal slip zone in the Wenchuan Earthquake Fault Scientific Drilling Project Hole-1 (WFSD-1): Tectonophysics 584 (0), 23-42.

Li, H., Zhang, Y., Dong, S., Zhang, J., Sun, Y. and Wang, Q., 2020. Neotectonics of the Bailongjiang and Hanan faults: New insights into late Cenozoic deformation along the eastern margin of the Tibetan Plateau. GSA Bulletin, 132(9-10): 1845-1862.

Li, S.K., Zhang, Y., Xiong, J., He, C., Ma, S., 2019. Evolution history of Cretaceous to Cenozoic structural tectonic field in the Huicheng Basin along the Qinling tectonic belt. Acta Geol. Sin. 93, 1885-1902.

Li, Y., Allen, P. A., Densmore, A. L., and Qiang, X., 2003, Evolution of the Longmen Shan foreland basin (western Sichuan, China) during the Late Triassic Indosinian orogeny: Basin Research 15 (1), 117-138.

Li, Z.-W., Liu, S., Chen, H., Deng, B., Hou, M., Wu, W., and Cao, J., 2012, Spatial variation in Meso-Cenozoic exhumation history of the Longmen Shan thrust belt (eastern Tibetan Plateau) and the adjacent western Sichuan basin: Constraints from fission track thermochronology: Journal of Asian Earth Sciences 47, 185-203.

Liu, B., Yuan, D., Zhang, B., Chen, W. and Niu, Y., 2012. Determination of fault parameters and sliding behavior of the 1879 southern Wudu M8.0 earthquake. Seismology and Geology, 34(3): 415–424.

Liu, X.-w., Yuan, D.-y., Shao, Y.-x. and Wu, Z., 2015. Characteristics of Late Quaternary Tectonic Activity in the Middle-eastern Segment of the Southern Branch of Diebu-Bailongjiang Fault, Gansu. Journal of Earch Sciences and Environment, 37(6): 111-119.

Liu-Zeng, J., Zhang, J., McPhillips, D., Reiners, P., Wang, W., Pik, R., Zeng, L., Hoke, G., Xie, K., and Xiao, P., 2018, Multiple episodes of fast exhumation since Cretaceous in southeast Tibet, revealed by low-temperature thermochronology: Earth Planetary Science Letters 490, 62-76.

Liu-Zeng, J., Zhang, Z., Wen, L., Tapponnier, P., Sun, J., Xing, X., Hu, G., Xu, Q., Zeng, L., and Ding, L., 2009, Co-seismic ruptures of the 12 May 2008, Ms 8.0 Wenchuan earthquake, Sichuan: East–west crustal shortening on oblique, parallel thrusts along the eastern edge of Tibet: Earth Planetary Science Letters 286 (3-4), 355-370.

Luo, L., Qi, J.-F., Jia, D., Wang, K., and Zeng, X., 2013, Magnetic fabric investigation in Tianquan-Leshan section in front of Longmenshan fold-thrust belt and its indicative significance for the Cenozoic deformation: Diqiu Wuli Xuebao 56 (2), 558-566.

Luo, L., Jia, D., Chen, Z., Hu, Q., Jia, Q., Li, Y., and Zhang, Y., 2006, Magnetic fabric evolution in the northwestern Sichuan basin, China and its strain characteristics: Geological Bulletin of China 25 (11), 1342-1348.

Molnar, P., Boos, W. R., and Battisti, D. S., 2010, Orographic controls on climate and paleoclimate of Asia: thermal and mechanical roles for the Tibetan Plateau: Annual Review of Earth Planetary Sciences 38, 77-102.

Molnar, P., and Tapponnier, P., 1975, Cenozoic tectonics of Asia: effects of a continental collision: Science 189 (4201), 419-426.

Montgomery, D.R., Brandon, M.T., 2002. Topographic controls on erosion rates in tectonically active mountain ranges. Earth Planet. Sci. Lett. 201, 481-489.

Ouimet, W., Whipple, K., Royden, L., Reiners, P., Hodges, K., and Pringle, M., 2010, Regional incision of the eastern margin of the Tibetan Plateau: Lithosphere 2 (1), 50-63.

Powell, C. M., and Conaghan, P., 1973, Plate tectonics and the Himalayas: Earth Planetary Science Letters 20 (1), 1-12.

Ratschbacher, L., Hacker, B. R., Calvert, A., Webb, L. E., Grimmer, J. C., McWilliams, M. O., Ireland, T., Dong, S., and Hu, J., 2003, Tectonics of the Qinling (Central China): tectonostratigraphy, geochronology, and deformation history: Tectonophysics 366 (1-2), 1-53.

Reiners, P. W., and Brandon, M. T., 2006, Using thermochronology to understand orogenic erosion: Annu. Rev. Earth Planet. Sci. 34, 419-466.

Ren, J., Xu, X., Yeats, R. S., and Zhang, S., 2013, Millennial slip rates of the Tazang fault, the eastern termination of Kunlun fault: Implications for strain partitioning in eastern Tibet: Tectonophysics 608, 1180-1200.

Richardson, N. J., Densmore, A. L., Seward, D., Fowler, A., Wipf, M., Ellis, M. A., Yong, L., and Zhang, Y., 2008, Extraordinary denudation in the Sichuan Basin: Insights from low-temperature thermochronology adjacent to the eastern margin of the Tibetan Plateau: Journal of Geophysical Research 113, doi:10.1029/2006JB004739.

Royden, L. H., Burchfiel, B. C., and van der Hilst, R. D., 2008, The Geological Evolution of the Tibetan Plateau: Science 321 (5892), 1054-1058.

Roberts, N. and Holdsworth, R., 2022. Timescales of faulting through calcite geochronology: A review. Journal of Structural Geology, 158: 104578.

SBGMR (Sichuan Bureau of Geology and Mineral Resources), 1991, Regional Geology of Sichuan Province, Beijing, Geol. Publ. House, 728

Sun, M., Yin, A., Yan, D., Ren, H., Mu, H., Zhu, L., and Qiu, L., 2018, Role of pre-existing structures in controlling the Cenozoic tectonic evolution of the eastern Tibetan plateau: New insights from analogue experiments: Earth and Planetary Science Letters 491, 207-215.

Tan, X., Liu, Y., Lee, Y.-H., Lu, R., Xu, X., Suppe, J., Shi, F., and Xu, C., 2019, Parallelism between the maximum exhumation belt and the Moho ramp along the eastern Tibetan Plateau margin: Coincidence or consequence?: Earth Planetary Science Letters 507, 73-84.

Tapponnier, P., Zhiqin, X., Roger, F., Meyer, B., Arnaud, N., Wittlinger, G., and Jingsui, Y., 2001, Oblique stepwise rise and growth of the Tibet Plateau: Science 294 (5547), 1671-1677.

Tian, Y., Kohn, B. P., Gleadow, A. J. W., and Hu, S., 2013, Constructing the Longmen Shan eastern Tibetan Plateau margin: Insights from low-temperature thermochronology: Tectonics 32 (3), 576-592.

Tian, Y., Kohn, B. P., Hu, S., and Gleadow, A. J. W., 2015, Synchronous fluvial response to surface uplift in the eastern Tibetan Plateau: Implications for crustal dynamics: Geophysical Research Letters 42 (1), 29-35.

Tian, Y., Kohn, B. P., Phillips, D., Hu, S., Gleadow, A. J. W., and Carter, A., 2016, Late Cretaceous-earliest Paleogene deformation in the Longmen Shan fold-and-thrust belt, eastern Tibetan Plateau margin: Pre-Cenozoic thickened crust?: Tectonics 35 (10), 2293-2312.

Tian, Y., Li, R., Tang, Y., Xu, X., Wang, Y., and Zhang, P., 2018, Thermochronological Constraints on the Late Cenozoic Morphotectonic Evolution of the Min Shan, the Eastern Margin of the Tibetan Plateau: Tectonics 37 (6), 1733-1749.

Vermeesch, P., 2018, IsoplotR: a free and open toolbox for geochronology: Geoscience Frontiers 9 (5), 1479-1493.

Vermeesch, P., and Tian, Y., 2014, Thermal history modelling: HeFTy vs. QTQt: Earth-Science Reviews 139, 279-290.

Wang, C., Feng, Z., Zhang, L., Huang, Y., Cao, K., Wang, P., Zhao, B., 2013. Cretaceous paleogeography and paleoclimate and the setting of SKI borehole sites in Songliao Basin, northeast China. Palaeogeogr. Palaeoclimatol. Palaeoecol. 385, 17-30.

Wang, C., Zhao, X., Liu, Z., Lippert, P. C., Graham, S. A., Coe, R. S., Yi, H., Zhu, L., Liu, S., and Li, Y., 2008, Constraints on the early uplift history of the Tibetan Plateau: Proceedings of the National Academy of Sciences 105 (13), 4987-4992.

Wang, C.-Y., Zhu, L., Lou, H., Huang, B.-S., Yao, Z., Luo, X., 2010. Crustal thicknesses and Poisson's ratios in the eastern Tibetan Plateau and their tectonic implications. J. Geophys. Res., 115, B11301, doi:10.1029/2010JB007527.

Wang, E., Kirby, E., Furlong, K. P., van Soest, M., Xu, G., Shi, X., Kamp), J. J., and Hodges, K. V., 2012, Two-phase growth of high topography in eastern Tibet during the Cenozoic: Nature Geoscience 5 (9), 640-645.

Wang, E., Meng, K., Su, Z., Meng, Q., Chu, J. J., Chen, Z., Wang, G., Shi, X., and Liang, X., 2014, Block rotation: Tectonic response of the Sichuan basin to the southeastward growth of the Tibetan Plateau along the Xianshuihe-Xiaojiang fault: Tectonics 33 (5), 686-718.

Wang, F., Shi, W., Zhang, W., Wu, L., Yang, L., Wang, Y., and Zhu, R., 2017, Differential growth of the northern Tibetan margin: evidence for oblique stepwise rise of the Tibetan Plateau: Scientific Reports 7), 41164.

Wang, Q., Qiao, X., Lan, Q., Freymueller, J., Yang, S., Xu, C., Yang, Y., You, X., Tan, K., Chen, G., 2011. Rupture of deep faults in the 2008 Wenchuan earthquake and uplift of the Longmen Shan. Nat. Geosci. 4, 634-640.

Wang, X., Zattin, M., Li, J., Song, C., Peng, T., Liu, S., Liu, B., 2011. Eocene to Pliocene exhumation history of the Tianshui-Huicheng region determined by Apatite fission track thermochronology: Implications for evolution of the northeastern Tibetan Plateau margin. J. Asian Earth Sci. 42, 97-110.

Wu, L., Lin, X., Cowgill, E., Xiao, A., Cheng, X., Chen, H., Zhao, H., Shen, Y., and Yang, S., 2019, Middle Miocene reorganization of the Altyn Tagh fault system, northern Tibetan Plateau: GSA Bulletin 131 (7-8), 1157-1178.

Xu, L., Rondenay, S., and van der Hilst, R. D., 2007, Structure of the crust beneath the southeastern Tibetan Plateau from teleseismic receiver functions: Physics of the Earth and Planetary Interiors 165 (3-4), 176-193.

Xu, M., Zhu, C., Tian, Y., Rao, S., Hu, S., 2011. Borehole temperature logging and characteristics of subsurface temperature in Sichuan Basin. Chin. J. Geophys. 54, 1052-1060.

Xu, X., Wen, X., Yu, G., Chen, G., Klinger, Y., Hubbard, J., and Shaw, J., 2009, Coseismic reverse- and oblique-slip surface faulting generated by the 2008 Mw 7.9 Wenchuan earthquake, China: Geology 37 (6), 515-518.

Xu, X., Wen, X., Han, Z., Chen, G., Li, C., Zheng, W., Zhnag, S., Ren, Z., Xu, C., and Tan, X., 2013, Lushan M S 7.0 earthquake: A blind reserve-fault event: Chinese Science Bulletin 58 (28-29), 3437-3443.

Xue, Z., Martelet, G., Lin, W., Faure, M., Chen, Y., Wei, W., Li, S., and Wang, Q., 2017, Mesozoic crustal thickening of the Longmenshan Belt (NE Tibet, China) by imbrication of basement slices: Insights from structural analysis, petrofabric and magnetic fabric studies, and gravity modeling: Tectonics 36 (12), 3110-3134.

Yan, D.-P., Zhou, M.-F., Li, S.-B., and Wei, G.-Q., 2011, Structural and geochronological constraints on the Mesozoic-Cenozoic tectonic evolution of the Longmen Shan thrust belt, eastern Tibetan Plateau: Tectonics 30, doi:10.1029/2011TC002867.

Yan, D. P., Qiu, L., Wells, M. L., Zhou, M. F., Meng, X., Lu, S., Zhang, S., Wang, Y., and Li, S. B., 2018, Structural and Geochronological Constraints on the Early Mesozoic North Longmen Shan Thrust Belt: Foreland Fold-Thrust Propagation of the SW Qinling Orogenic Belt, Northeastern Tibetan Plateau: Tectonics 37 (12), 4595-4624.

Yang, Z., Shen, C., Ratschbacher, L., Enkelmann, E., Jonckheere, R., Wauschkuhn, B., and Dong, Y., 2017, Sichuan Basin and beyond: Eastward foreland growth of the Tibetan Plateau from an integration of Late Cretaceous-Cenozoic fission track and (U-Th)/He ages of the eastern Tibetan Plateau, Qinling, and Daba Shan: Journal of Geophysical Research: Solid Earth 122 (6), 4712-4740.

Yin, A., 2010, A special issue on the great 12 May 2008 Wenchuan earthquake (Mw7.9): Observations and unanswered questions: Tectonophysics 491 (1), 1-9.

Yin, A., and Harrison, T. M., 2000, Geologic Evolution of the Himalayan-Tibetan Orogen: Annual Review of Earth and Planetary Sciences 28 (1), 211-280.

Yu, G., Xu, X., Klinger, Y., Diao, G., Chen, G., Feng, X., Li, C., Zhu, A., Yuan, R., Guo, T., Sun, X., Tan, X., and An, Y., 2010, Fault-Scarp Features and Cascading-Rupture Model for the Mw 7.9 Wenchuan Earthquake, Eastern Tibetan Plateau, China: Bulletin of the Seismological Society of America 100 (5B), 2590-2614.

Zhang, G., Tian, Y., Li, R., Shen, X., Zhang, Z., Sun, X. and Chen, D., 2022. Progressive tectonic evolution from crustal shortening to mid-lower crustal expansion in the southeast Tibetan Plateau: A synthesis of structural and thermochronological insights. Earth-Science Reviews, 226: 103951.

Zhang, H., Yi, G., Zhang, P. and Kirby, E., 2015. On the evolution of seismogenic faults in the Longmen Shan, eastern Tibet. Journal of Asian Earth Sciences, 111: 624-631.

Zhang, H.-p., Zhang, P.-z., Kirby, E., Yin, J.-h., Liu, C.-r. and Yu, G.-h., 2011. Along-strike topographic variation of the Longmen Shan and its significance for landscape evolution along the eastern Tibetan Plateau. Journal of Asian Earth Sciences, 40(4): 855-864.

Zhang, P.-Z., Wen, X.-z., Shen, Z.-K., and Chen, J.-h., 2010, Oblique, High-Angle, Listric-Reverse Faulting and Associated Development of Strain: The Wenchuan Earthquake of May 12, 2008, Sichuan, China: Annual Review of Earth and Planetary Sciences 38 (1), 353-382.

Zhang, Y.-P., Zheng, W.-J., Wang, W.-T., et al., 2020. Rapid Eocene Exhumation of the West Qinling Belt: Implications for the Growth of the Northeastern Tibetan Plateau. Lithosphere 2020, 1-12.

Zhang, Z., Wang, Y., Chen, Y., Houseman, G. A., Tian, X., Wang, E., and Teng, J., 2009, Crustal structure across Longmenshan fault belt from passive source seismic profiling: Geophys. Res. Lett., 36, L17310, doi:10.1029/2009GL039580.

Zhu, A., Xu, X., Diao, G., Su, J., Feng, X., Sun, Q., and Wang, Y., 2008, Relocation of the Ms 8.0 Wenchuan earthquake sequence in part: Preliminary seismotectonic analysis: Seismology Geology 30 (3), 759-767.

Zhuang, G., Johnstone, S. A., Hourigan, J., Ritts, B., Robinson, A., and Sobel, E. R., 2018, Understanding the geologic evolution of Northern Tibetan Plateau with multiple thermochronometers: Gondwana Research 58, 195-210.

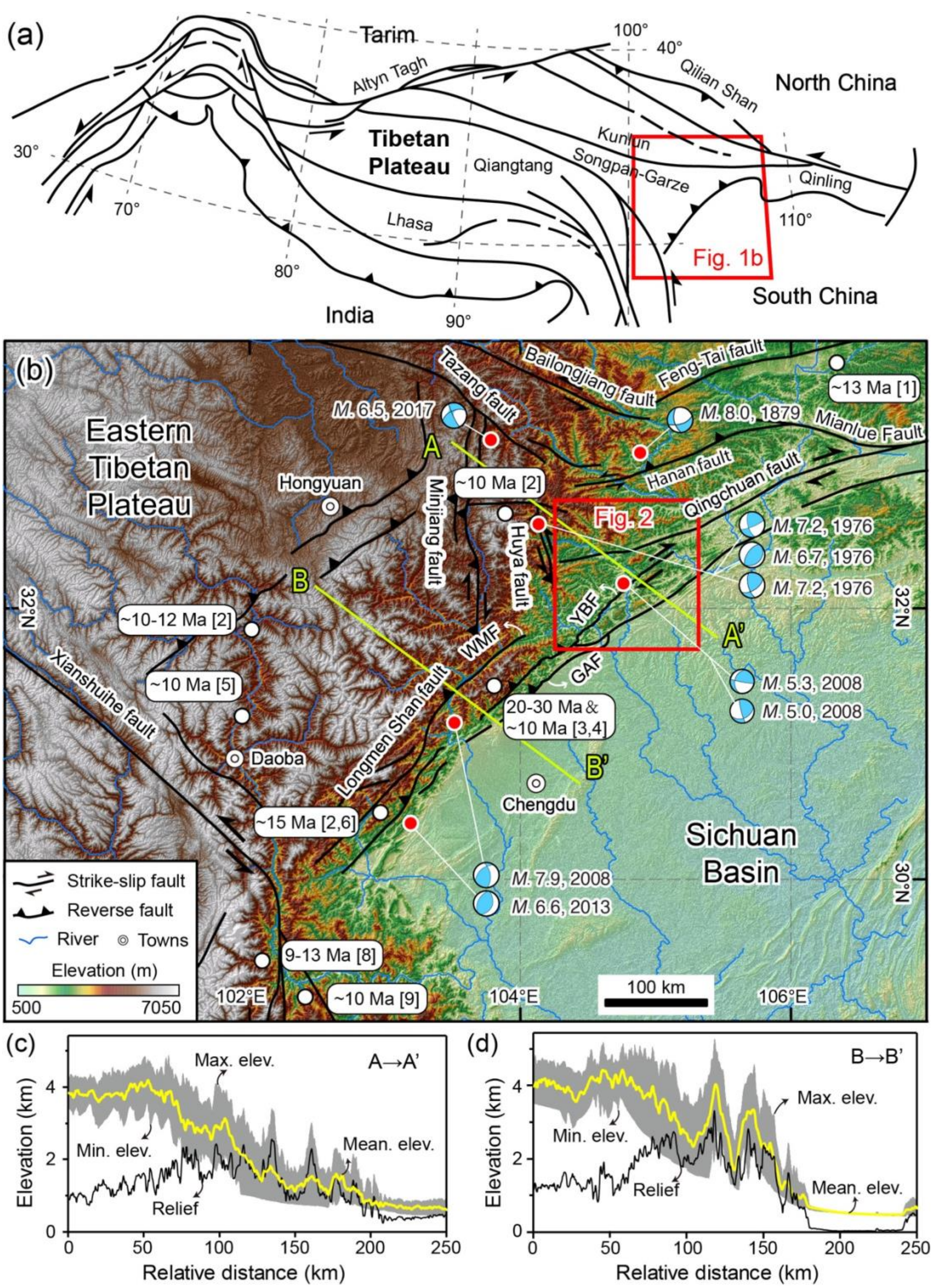

Fig. 1. (a) Tectonic framework of the Tibetan Plateau, showing the location of the study area (red rectangle). (b) SRTM map showing regional topography, rivers and the primary fault system of the eastern Tibetan Plateau, in which the study area is marked by the red rectangle. Also compiled in this panel is the onset time of rock exhumation at different sectors, marked by white circles. Reference codes are as follows: [1] Yang

et al. (2017); [2] Tian et al. (2013, 2015, 2018); [3] Wang et al. (2012); [4] Godard et al. (2009); [5] Ouimet et al. (2010); [6] Cook et al. (2013); [7] Richardson et al. (2008); [8] Clark et al. (2005b); [9] Deng et al. (2014). Focal mechanisms sourced from Global Centroid Moment Tensor Catalog and Shan et al. (2015). (c) and (d) Topographic swath across the northern Longmen Shan along the A-A' and B-B' transect, marked in panel (b). Maximum, minimum, mean elevation and relief are calculated using a swath width of 10 km. Abbreviations: GAF=Guanxian-Anxian Fault; WMF=Wenchuan-Maowen Fault, YBF=Yingxiu-Beichuan Fault.

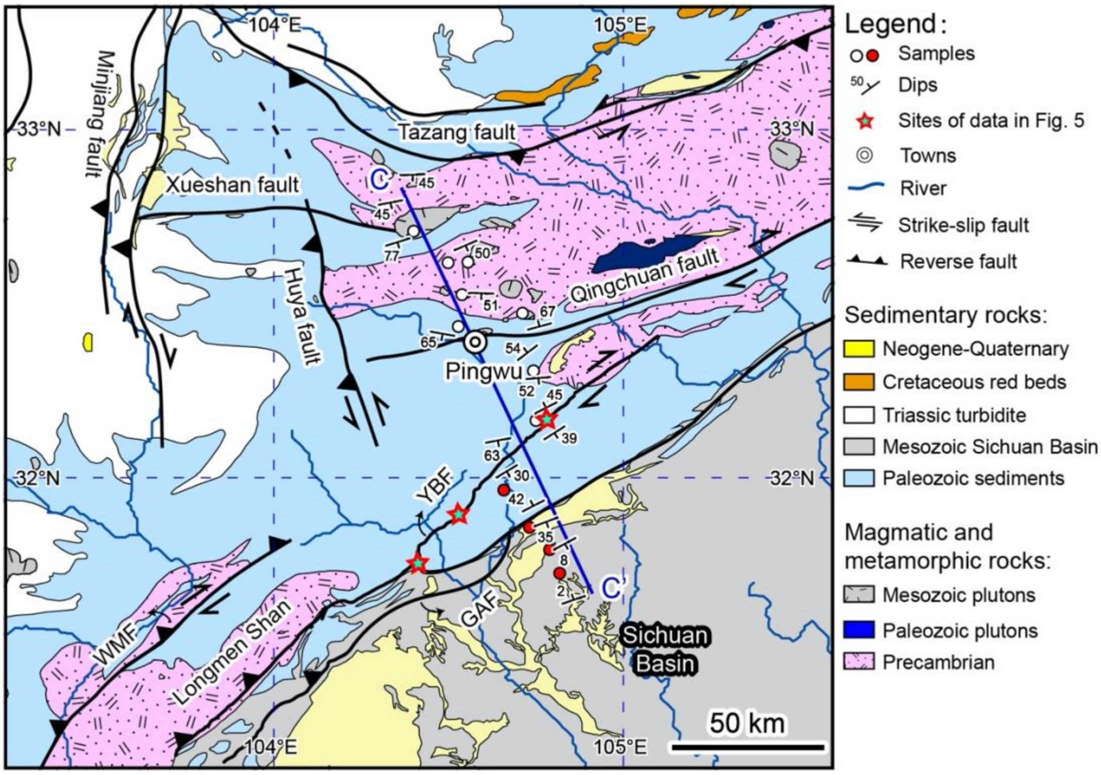

Fig. 2. Generalized geological map, showing major structures and lithologies of the study area (SBGMR, 1991). Locations of the Yingxiu-Beichuan and Guanxian-Anxian faults, ruptured by the Wenchuan fault, source from Liu-Zeng et al. (2009). Samples were collected from Mesozoic plutons, Precambrian, Paleozoic sediments and Mesozoic clastic sediments along the C-C' horizontal profile. See Fig. 3 for sample names and thermochronological results. See Fig. 4 for the geological and thermochronological transects.

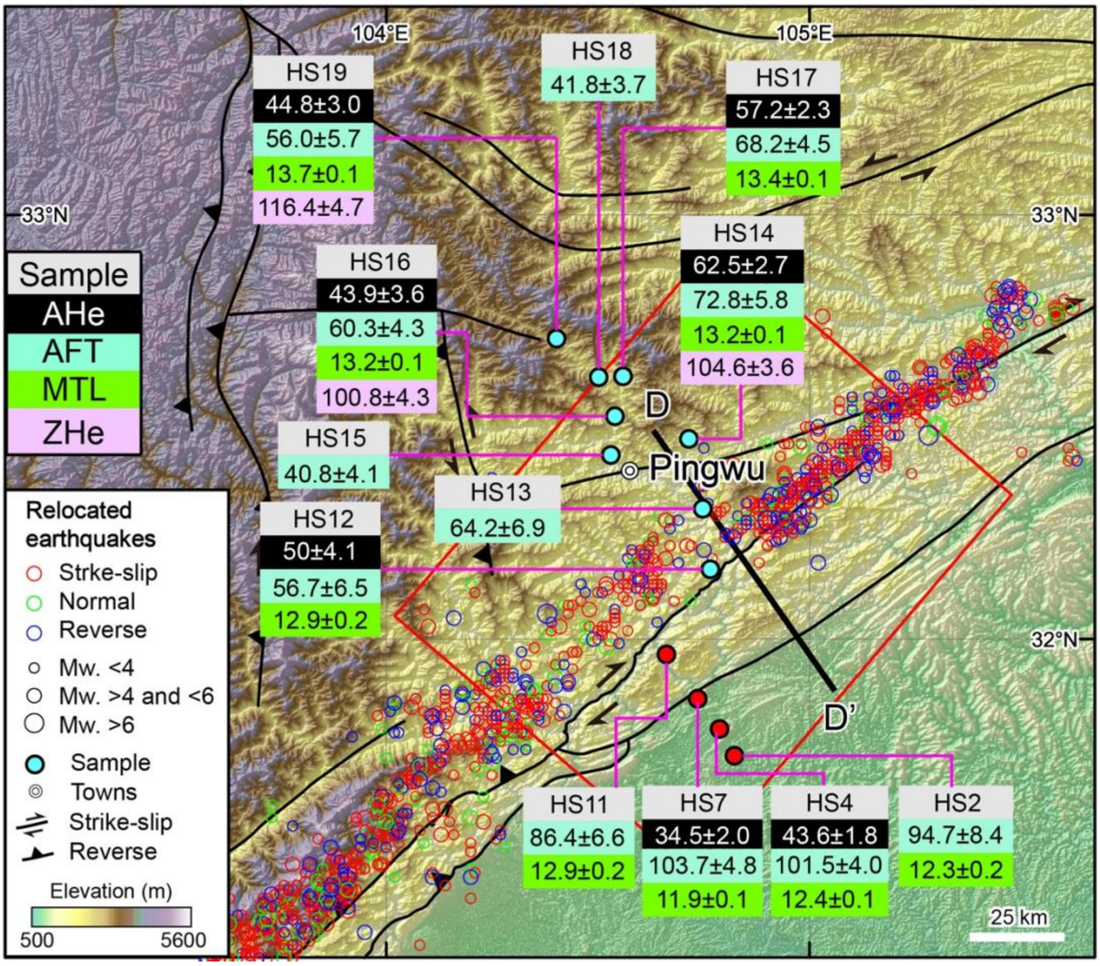

Figure. 3. SRTM Digital elevation model of the study area, showing the AFT, AHe, MTL and ZHe results of samples reported in this work. See Fig. 2 for fault names. Red, green and blue circles show the relocated epicenters of strike-slip, normal and reverse aftershocks of the Wenchuan earthquake (Yu et al., 2010). D-D' black line marks the location of a seismic profile shown in Fig. 4a. The red rectangle denotes the area plotted in Fig. 4b. Note that AFT ages of the samples HS15-HS19 were sourced from Tian et al. (2018).

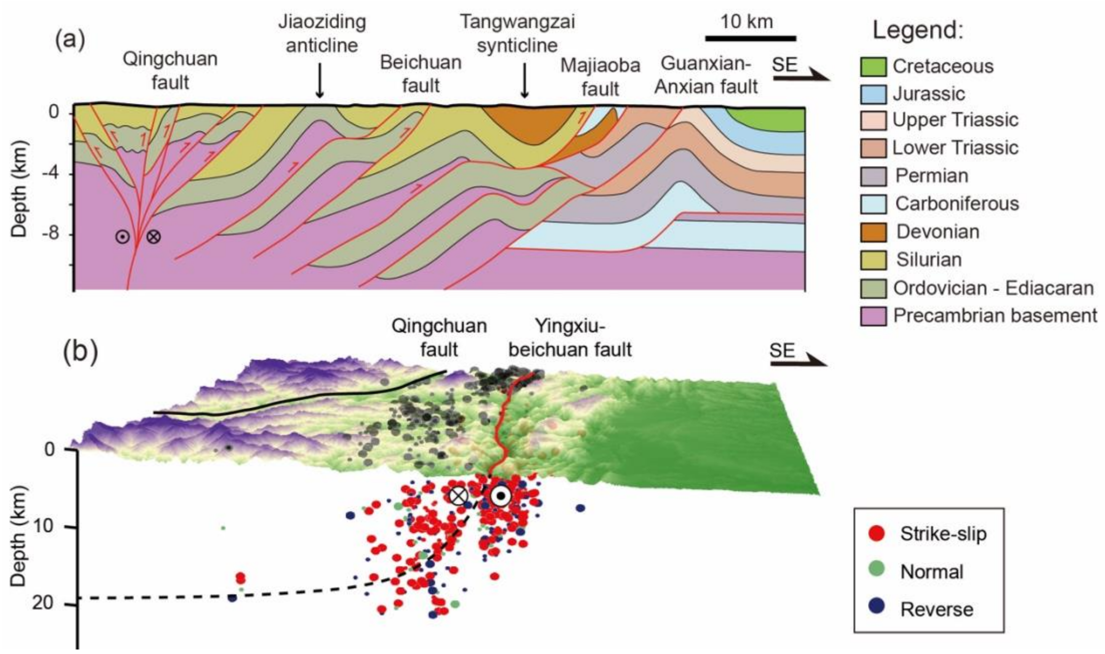

Fig. 4. (a) A seismic profile (D-D' in Fig. 3) across the northern segment of the Longmen Shan, showing a positive flow structure rooting into the Qingchuan fault, modified from Jia et al. (2006). (b) A 3D diagram showing the relocated foci and epicenters of aftershocks of the Wenchuan earthquake in the northern Longmen Shan. See Fig. 3 for a map view of these events. Earthquake foci, sourced from Yu et al. (2010), are color coded by focal mechanism. The dash curve in panel b marks the interpreted fault.

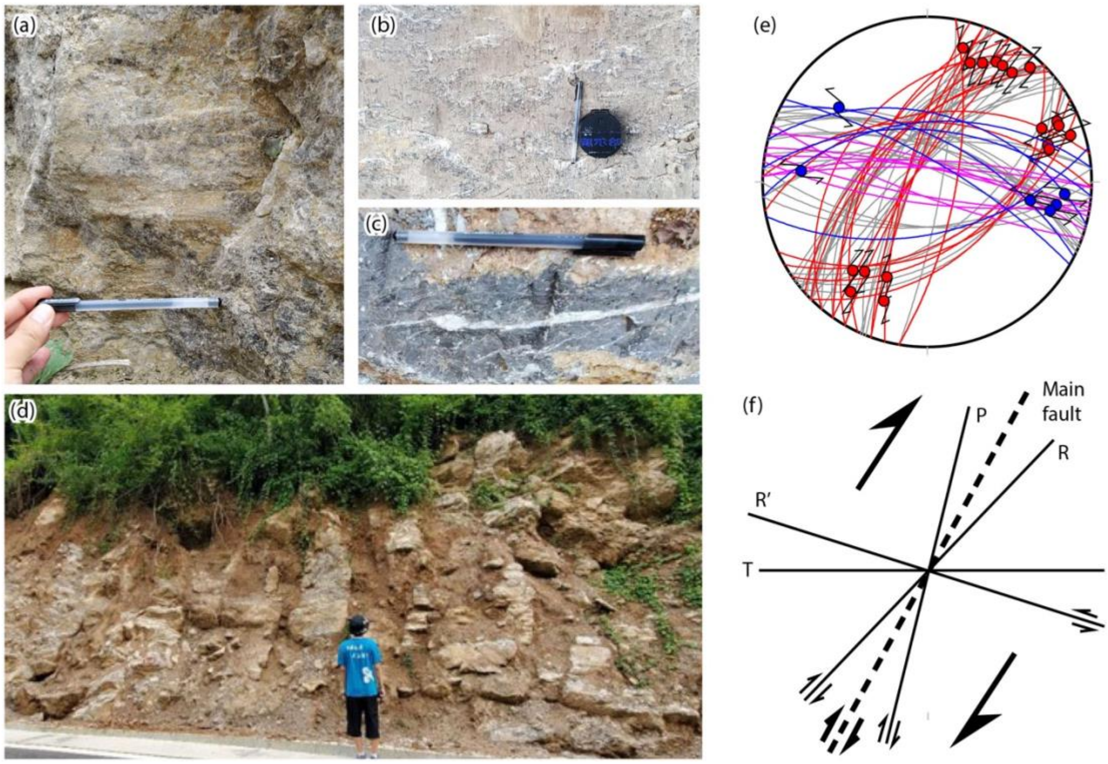

Fig. 5. (a) A northwestward view of representative outcrops of fault breccia hosting slickensides on which horizontal strike-slipping striations developed. (b) A northeastward view of representative SE-striking slickensides with sub-vertical top-down normal striations. (c) A downward view of brittle fractures (filled by calcite), indicating right-lateral slip. (d) A northeastward view of vertical ESE-striking extensional fractures. (e) Schmidt's stereonets of slickensides and striations with red pairs for right-lateral strike-slipping, blue for left-lateral, purple for extensional joints and gray ones without unambiguous slipping senses. These measurements are presented in Supplementary Data TS1. (f) Schematics of Rediel shears (modified after Tchalenko, 1970) for explaining the observed faults with different senses of shear, compiled in panel d. In the study area, right-lateral strike-slip faults correspond to the R and P structures, left-lateral ones are R' shears (blue in panel d), and those extensional fractures (c, purple in panel d) are tensional joints.

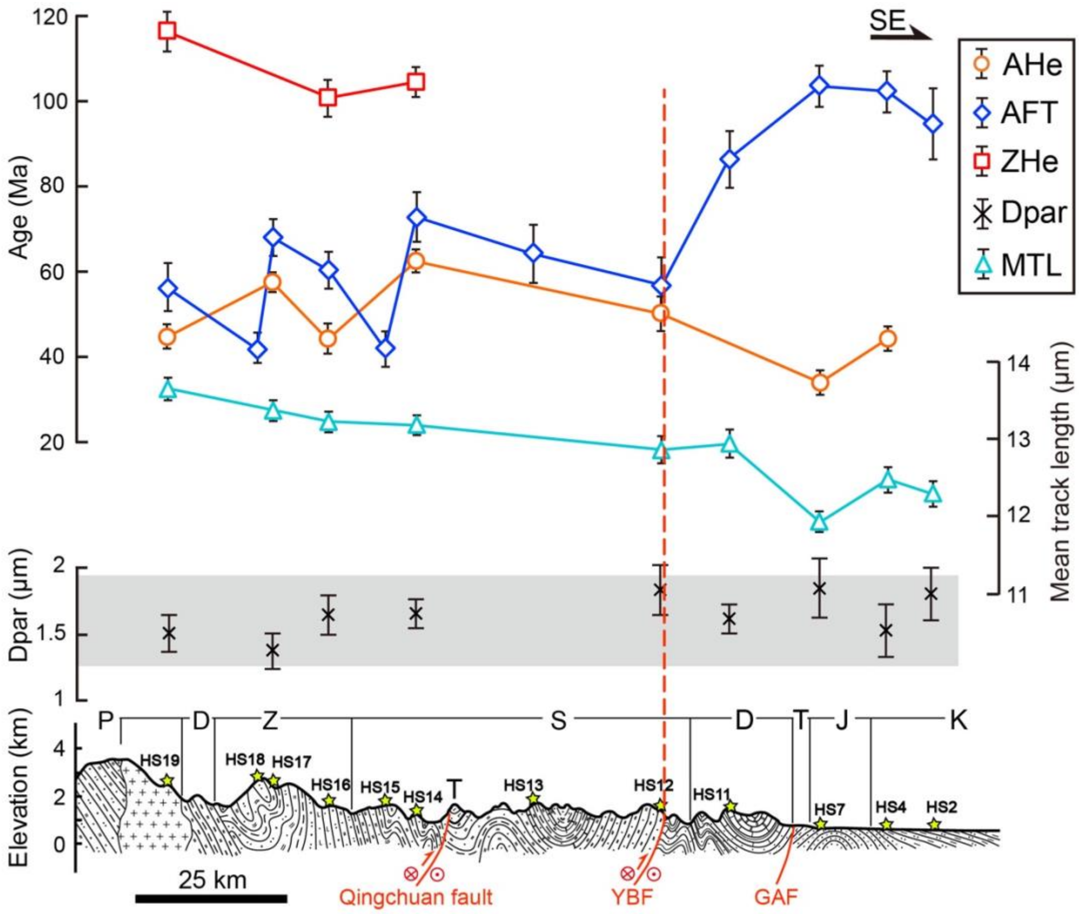

Figure. 6. Plot of AHe, ZHe, AFT ages, AFT mean length, Dpar of samples along the transect C-C' (lowest panel, see Fig. 3 for transect location). AFT ages and mean lengths west of the Yingxiu-Beichuan fault (YBF) are systematically different from those from the east. No systematic age changes have been observed across other faults.

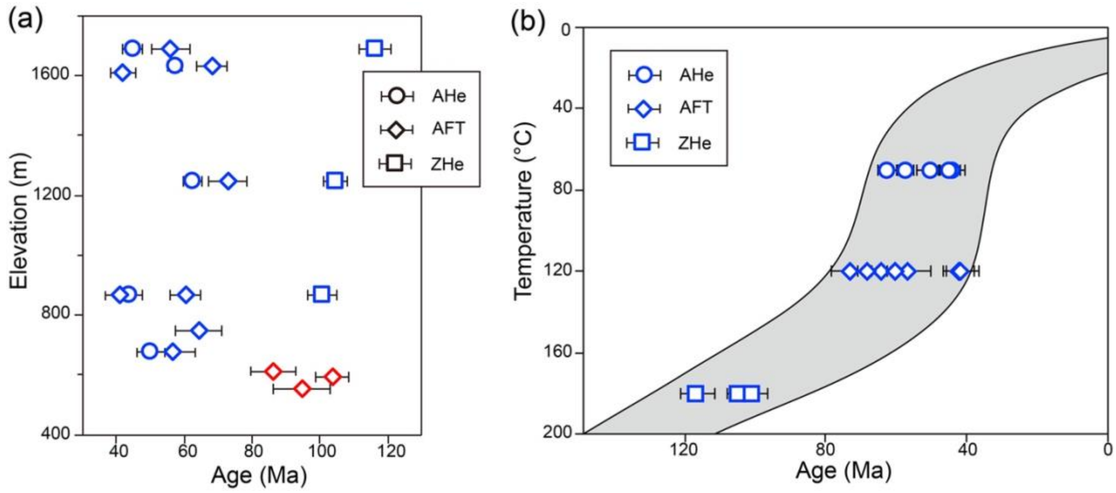

Fig. 7. (a) AHe, AFT and age-elevation plot for samples located to the west (blue) and east (red) of the YBF. (b) Plot of different thermochronometers versus their closure temperatures and the present temperature. The envelope shows an early Cretaceous - Eocene phase of enhanced cooling followed by decreased cooling. The closure temperature of AHe, AFT and ZHe are 70 °C, 120 °C and 180 °C, respectively (Reiners and Brandon, 2006 and references therein).

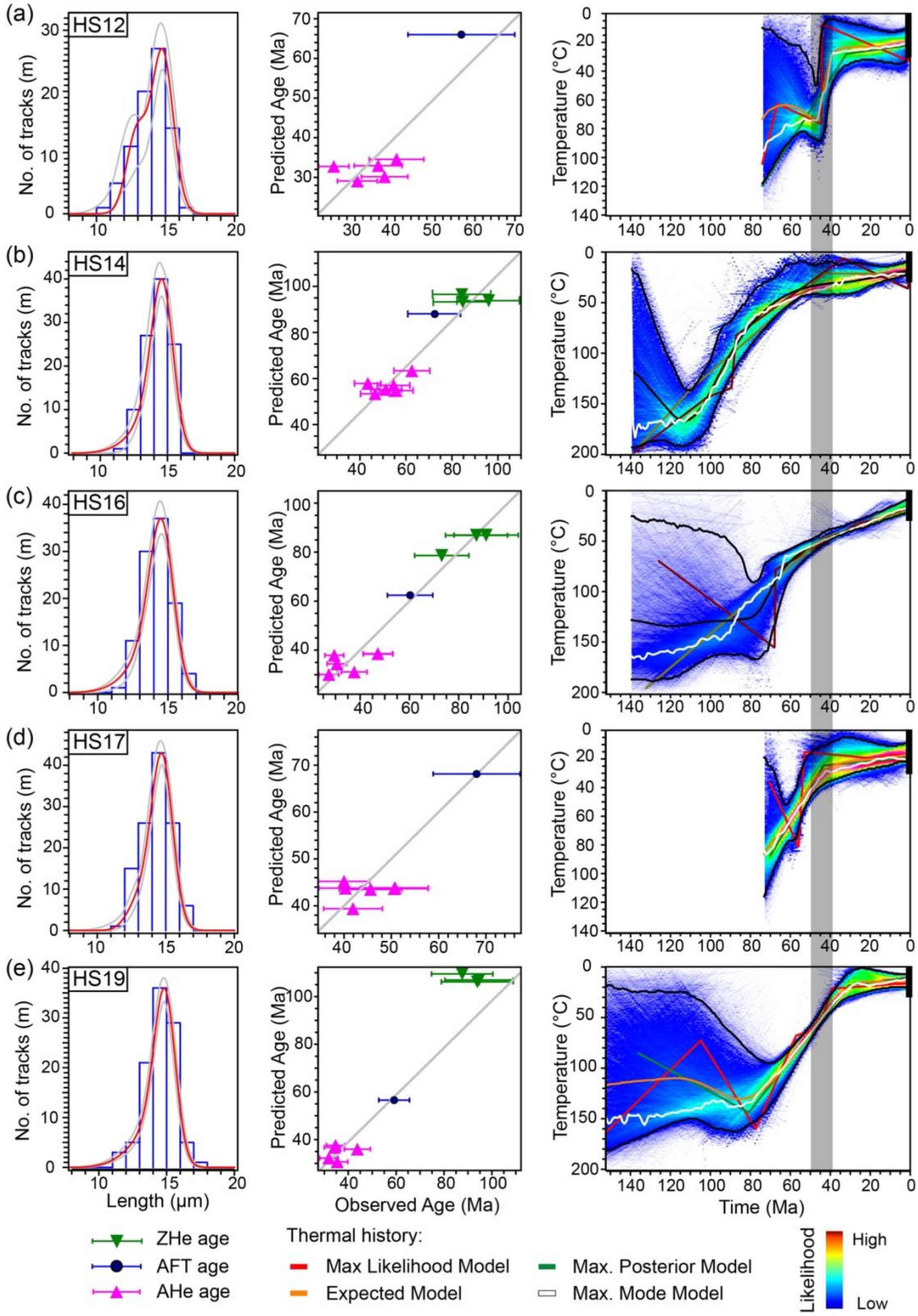

Fig. 8. Thermal history modeling results for samples west of the Yingxiu-Beichuan fault (right panel), comparison plots between observed and modelled AFT length distribution (left panel) and ages (central panel). The expected model is an effectively weighted mean model, where the weighting is provided by the posterior probability for

each model. The two black lines show the 95% credible intervals of the expected model. The maximum likelihood model is the best data fitting model. The maximum posterior model is sensitive to the range of the prior specified for the general thermal history model. The maximum mode model is the temperature value at each one-million-year step that has the greatest number of paths passing through it. The thick vertical line marks the present temperature (15 ± 15°C). The vertical gray area in the left column marks the time range of 50-40 Ma.

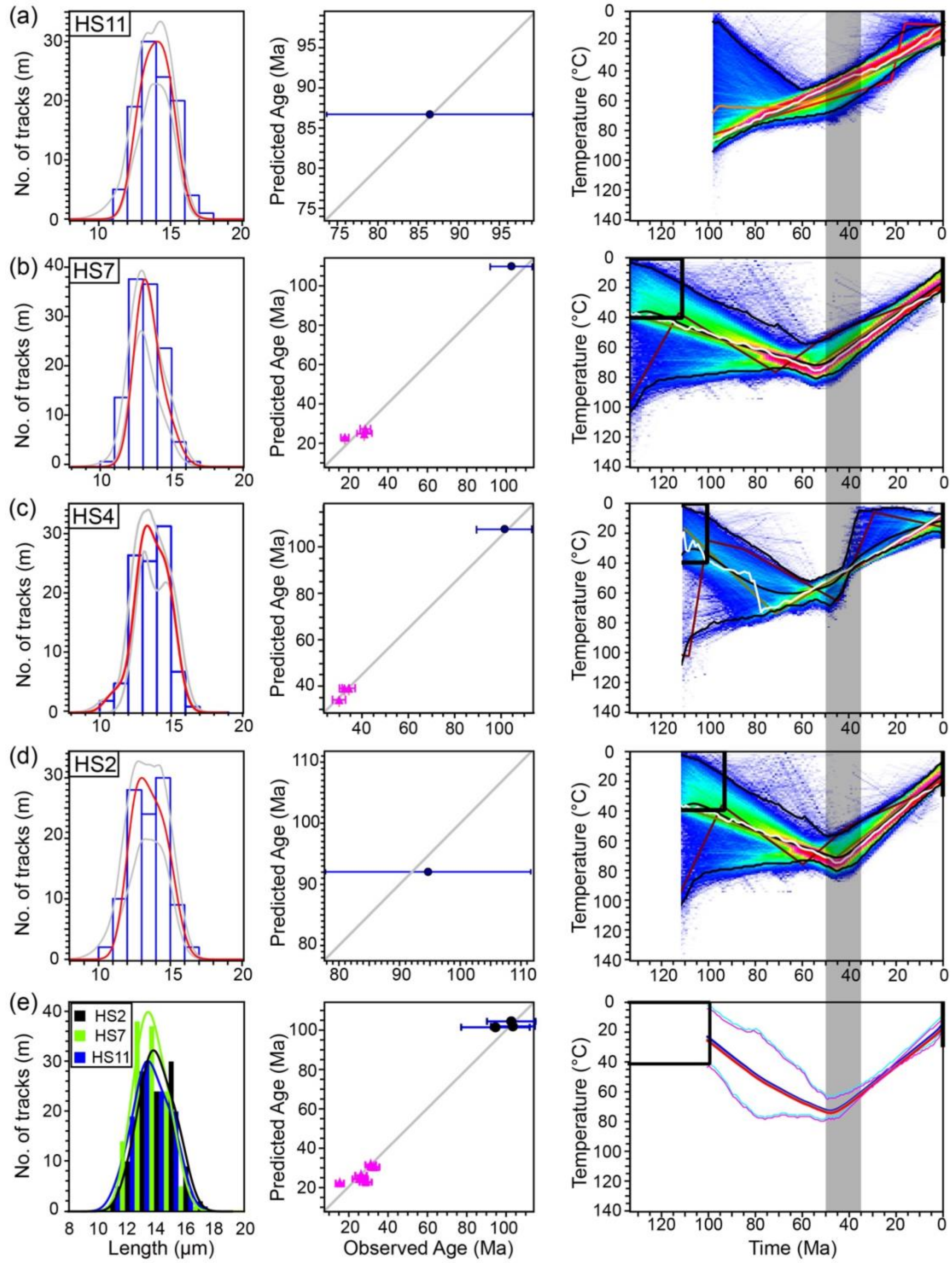

Fig. 9. Thermal history modeling results for samples (HS11, HS7, HS4 and HS2) east of the Yingxiu-Beichuan fault. Explanations for elements of panels a-d are the same as the Fig. 6. (d) Joint modeling combining HS2, HS7 and HS11. In this panel, black box mark geological constraints for the uppermost sample. The thermal history of the HS2 is plotted in blue, the HS7 in red, and intermediate sample HS4 in gray. Thin blue lines depict 95% credible intervals of the thermal history of HS2; whereas, thin red lines the

95% credible intervals of HS7.

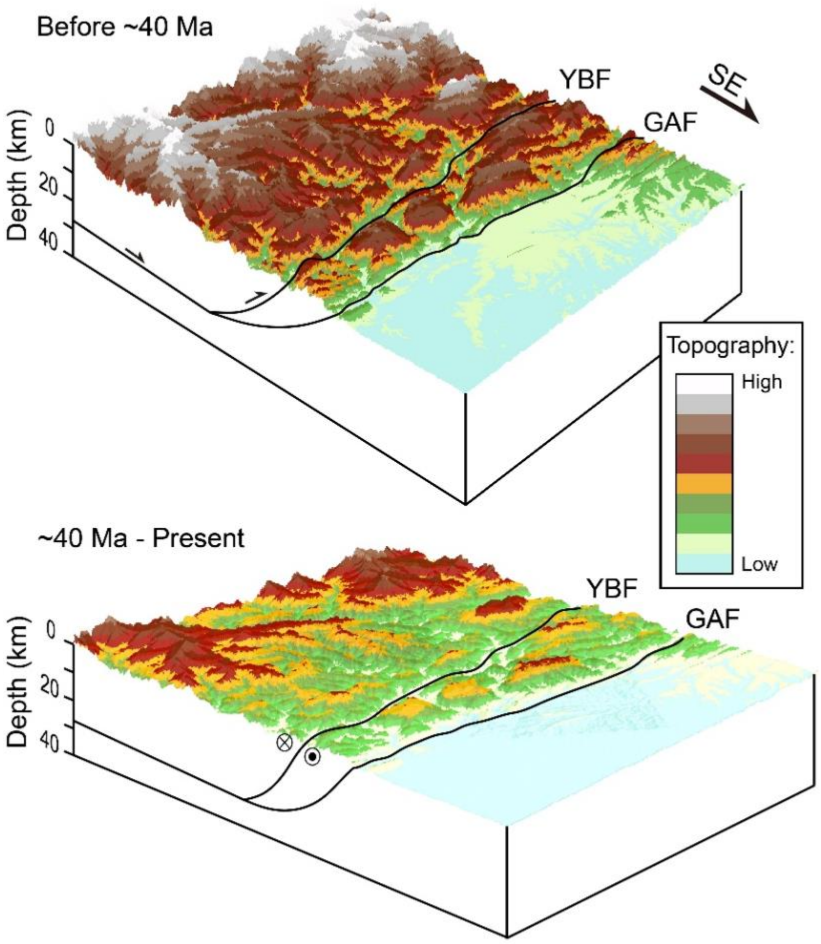

Fig. 10. Schematic diagrams showing the evolution of the northern Longmen Shan. Prior to the Eocene, reverse faults dominated the northern Longmen Shan. These accommodated significant amounts of upper crustal shortening, inducing rock uplift and exhumation west of the fault before ~50-40 Ma. Later deformation evolved to right-lateral shear with minor reverse faulting, similar to Quaternary deformation. This transition explains the observed minimum post-Eocene cooling and exhumation west of the Yingxiu-Beichuan fault. It reduced tectonic loading over the western margin of the Sichuan Basin, resulting in crustal isostatic rebound and the observed onset of exhumation east of the Yingxiu-Beichuan fault.

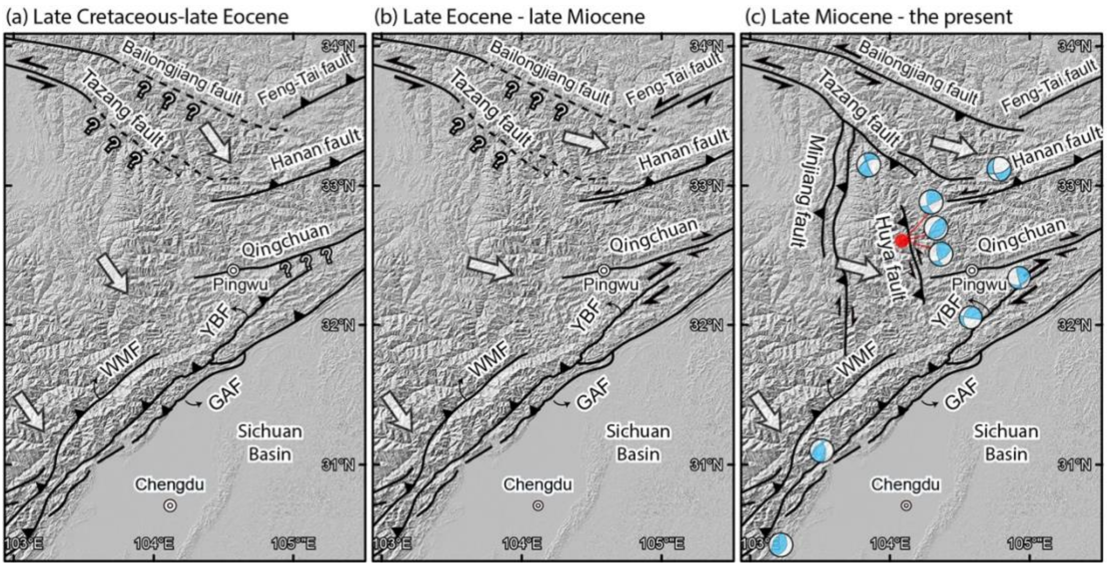

Fig. 11. Late Cretaceous – Cenozoic deformation sequence of faults in the eastern Tibetan Plateau. (a) During late Cretaceous – late Eocene, mapped deformation includes shortening structures in the LMSFZ, Feng-Tai and Hanan fault, indicating a regional NW-SE contractional stress-field. As the Sichuan Basin is likely stable, such a contraction likely results from SE-verging shortening. (b) Late Eocene time witnessed the onset of right-lateral slip along the Feng-Tai, Hanan, Qingchuan and the northern segment of the Yingxiu-Beichuan faults, which suggest the stress regime in the area may have transferred to be oblique to the LMSFZ. (c) South-trending oblique Minjiang and Huya reverse faults initiated at the late Miocene. Such oblique slip has also occurred on other adjacent faults as shown by focal mechanisms of major earthquakes with magnitudes more than 5 (see Fig. 1 for details).

Table 1. Sample information and results of apatite fission-track analysis

Sample information					Age Results						Track Length		
Sample No.	Lithology	Longitude, Latitude, Altitude			No. of Grains (n)	Spontaneous tracks		aPooled ^{238}U (ppm)	Disper-sion (%)	bCentral age (Ma±1σ)	Nonprojected		
		(°E)	(°N)	(m)		No. (n)	Density (10^6 cm^{-2})				cMean (µm±SE)	dSD (µm)	(µ
Eastern of the Yingxiu-Beichuan fault													
HS2	Lower Cretaceous sandstone	104.823	31.724	554	26	851	0.7978	17.2	40	94.7 ± 8.4	12.3 ± 0.2	1.6	1
HS4	Lower Cretaceous sandstone	104.801	31.768	560	25	1362	0.8551	20.1	36	101.5 ± 4.0	12.4 ± 0.1	1.4	1
HS7	Upper Jurassic sandstone	104.736	31.859	593	28	1485	0.8442	14.0	16	103.7 ± 4.8	11.9 ± 0.1	1.4	1
HS11	Devonian sandstone	104.663	31.963	612	25	2785	2.2385	49.4	34	86.4 ± 6.6	12.9 ± 0.2	1.8	1
Western of the Yingxiu-Beichuan fault													
HS12	Silurian sandstone	104.794	32.129	675	24	125	0.2926	10.2	25	56.7 ± 6.5	12.9 ± 0.2	1.6	1
HS13	Precambrian sandstone	104.749	32.306	747	24	134	0.2478	8.9	23	64.2 ± 6.9	-	-	
HS14	Mesozoic granite	104.716	32.471	1246	24	167	0.07792	2.1	0	72.8 ± 5.8	13.2 ± 0.1	1.3	1
HS15	Devonian sandstone	104.531	32.433	865	20	150	0.1842	9.0	15	40.8 ± 4.1*	-	-	
HS16	Mesozoic granite	104.541	32.524	867	27	261	0.1032	3.5	14	60.3 ± 4.3*	13.2 ± 0.1	1.4	1
HS17	Mesozoic granite	104.560	32.619	1631	34	640	0.4634	14.0	12	68.2 ± 4.5*	13.4 ± 0.1	1.4	1
HS18	Precambrian meta-sandstone	104.503	32.617	1608	21	132	0.1239	5.9	19	41.8 ± 3.7*	-	-	
HS19	Mesozoic granite	104.403	32.708	1688	25	958	0.7038	18.9	16	56.0 ± 5.7*	13.7 ± 0.1	1.5	1

[a] Pooled uranium content of all grains measured by LA-ICP-MS method.

[b] Central age calculated using the IsoplotR of Vermeesch (2018) and the method of Galbraith (2005).

[c] SE = standard error;

[d] SD = standard deviation;

[e] Number of track length measured.

* These AFT ages were reported in Tian et al. (2018).

Table 2. Results of apatite and zircon (U-Th-Sm)/He dating

Sample	Grain length (μm)	Grain width (μm)	^{4}He (ncc)	Mass (mg)	[a]Mean F_T	U (ppm)	Th (ppm)	Sm (ppm)	Th/U	[b]eU	Raw age (Ma)	Corrected age (Ma)	Er (±
AHe results													
Eastern of the Yingxiu-Beichuan fault													
HS4-1*	168.9	142.3	2.1449	0.0083	0.74	36.6	12.3	-	0.3	39.5	53.7	69.6	2
HS4-2	177.7	130.8	0.3283	0.0085	0.74	5.9	16.2	-	2.7	9.7	32.9	43.2	1
HS4-3	173.2	143.4	0.2387	0.0088	0.75	5.8	3.0	-	0.5	6.5	34.4	44.4	1
HS4-4*	204.9	123.9	0.1310	0.0107	0.76	1.7	2.8	-	1.7	2.4	42.8	54.9	2
HS4-5	158.0	94.2	0.0922	0.0048	0.68	2.7	10.7	-	4.0	5.2	30.4	43.2	1
HS7-1*	128.4	86.1	0.3682	0.0029	0.63	12.0	20.4	-	1.7	16.8	61.9	93.6	2
HS7-2	122.2	94.8	0.0752	0.0029	0.63	2.0	33.1	-	16.6	9.8	21.7	33.7	1
HS7-3*	127.5	78.0	0.5166	0.0026	0.61	21.6	19.6	-	0.9	26.2	62.4	95.9	3
HS7-4	118.9	84.2	0.0457	0.0024	0.61	4.0	20.2	-	5.0	8.8	17.6	27.8	1
HS7-5	124.7	79.0	0.1385	0.0025	0.61	7.7	35.7	-	4.6	16.1	28.1	44.5	1
HS7-6	122.3	88.8	0.0887	0.0027	0.63	7.6	9.0	-	1.2	9.7	27.7	42.0	1
Western of the Yingxiu-Beichuan fault													
HS12-1	144.0	75.4	0.230	0.0020	0.62	28.2	8.7	31.5	0.3	30.3	30.6	46.0	2
HS12-2	172.6	86.7	0.240	0.0032	0.68	14.0	9.9	33.1	0.7	16.3	37.4	52.8	2
HS12-3	148.7	71.0	0.300	0.0019	0.61	28.2	19.0	45.8	0.7	32.7	40.4	62.3	3
HS12-4	150.3	72.3	0.209	0.0019	0.61	19.4	18.8	616.7	1.0	23.8	35.8	54.9	3
HS12-5*	210.2	109.3	0.433	0.0062	0.74	3.3	1.5	1.5	0.5	3.6	153.7	200.0	1
HS12-6*	193.1	107.4	1.699	0.0055	0.73	33.5	2.1	2.1	0.1	34.0	73.7	96.5	5
HS12-7	162.4	82.1	0.553	0.0027	0.66	66.3	5.1	67.7	0.1	67.5	24.7	35.4	1
HS14-1	268.8	158.6	0.718	0.0168	0.82	6.6	5.9	95.3	0.9	8.0	43.4	52.0	2
HS14-2	275.8	144.1	0.405	0.0142	0.80	2.6	6.3	70.1	2.4	4.1	55.8	68.2	3
HS14-3	243.5	141.4	0.219	0.0121	0.80	2.1	4.5	56.0	2.2	3.1	46.6	57.5	3
HS14-4	308.4	154.8	0.616	0.0183	0.82	3.7	5.2	117.8	1.4	4.9	54.7	65.6	3
HS14-5	446.4	205.9	1.186	0.0470	0.87	2.2	4.3	101.5	2.0	3.2	62.7	71.6	3
HS14-6*	254.8	99.7	0.001	0.0063	0.73	5.2	13.0	99.8	2.5	8.3	0.2	0.3	0
HS14-7	350.3	139.4	0.409	0.0169	0.81	2.7	4.3	102.5	1.6	3.7	51.4	62.4	3
HS16-1	489.1	175.2	0.708	0.0373	0.85	2.3	3.8	77.2	1.6	3.2	47.2	54.8	3
HS16-2	425.7	177.5	0.496	0.0333	0.85	1.9	2.5	55.5	1.3	2.5	47.3	55.0	3
HS16-3	437.4	168.9	0.502	0.0310	0.84	3.4	4.2	83.9	1.2	4.4	29.5	34.4	1
HS16-4	281.5	105.6	0.139	0.0078	0.75	3.6	7.2	75.6	2.0	5.3	27.3	35.6	2
HS16-5	242.9	119.2	0.169	0.0086	0.77	2.7	6.6	70.5	2.5	4.2	37.6	48.0	2
HS16-6*	292.6	140.3	0.703	0.0143	0.80	2.6	5.4	73.2	2.1	3.9	101.4	124.0	6

HS16-7	316.7	141.5	0.202	0.0157	0.81	2.4	4.3	59.3	1.8	3.4	30.6	37.2	2
HS17-1	283.4	119.2	0.891	0.0101	0.78	15.8	9.3	n.d.	0.6	17.9	40.3	51.7	2
HS17-2	190.8	123.7	1.040	0.0073	0.77	22.9	11.2	n.d.	0.5	25.6	45.6	59.4	3
HS17-3	201.3	126.7	1.044	0.0081	0.77	18.9	8.4	n.d.	0.4	20.9	50.6	65.4	3
HS17-4	245.1	145.0	0.781	0.0129	0.81	10.7	7.1	n.d.	0.7	12.4	40.0	49.6	2
HS17-5	149.8	108.8	0.205	0.0044	0.72	7.6	6.0	94.7	0.8	9.0	41.9	56.1	3
HS17-6*	156.8	103.7	0.247	0.0042	0.72	13.9	11.0	n.d.	0.8	16.4	29.1	40.4	2
HS17-7*	192.7	92.3	0.208	0.0041	0.70	22.9	20.9	174.8	0.9	27.8	14.9	20.5	1
HS17-8	250.8	130.1	0.706	0.0105	0.78	9.3	5.7	102.0	0.6	10.7	50.8	63.1	3
HS19-1	202.6	89.2	0.251	0.0056	0.71	9.0	5.8	72.1	0.6	10.4	35.4	48.0	2
HS19-2	206.9	101.3	0.351	0.0075	0.74	9.9	8.9	74.0	0.9	12.0	31.9	41.7	1
HS19-3	395.8	129.3	1.841	0.0101	0.78	40.5	10.0	232.6	0.2	42.9	34.7	43.1	1
HS19-4	270.1	125.1	1.683	0.0105	0.78	28.3	6.2	190.0	0.2	29.8	43.8	54.5	2
HS19-5*	285.3	103.4	1.325	0.0076	0.74	14.9	13.3	164.7	0.9	18.1	78.3	101.9	5
HS19-6	257.9	138.9	1.397	0.0123	0.79	25.7	5.1	150.6	0.2	26.9	34.2	41.9	2
ZHe results													
Western of the Yingxiu-Beichuan fault													
HS14-1	203.5	102.9	0.143	0.0066	0.79	675.4	180.1	-	0.3	717.7	85.1	104.7	6
HS14-2	252.4	133.7	0.142	0.0135	0.83	366.2	137.7	-	0.4	398.5	96.4	113.3	6
HS14-3*	265.1	79.9	30.113	0.0052	0.75	404.0	249.3	-	0.6	462.6	101.3	135.6	8
HS14-4	322.8	135.1	0.142	0.0196	0.84	295.1	108.6	-	0.4	320.6	84.5	98.1	5
HS16-1	257.1	124.8	0.143	0.0125	0.82	293.2	151.9	-	0.5	328.9	91.1	107.9	6
HS16-2	302.1	84.1	0.143	0.0081	0.77	316.3	167.1	-	0.5	355.6	73.1	91.7	5
HS16-3*	348.7	69.8	39.060	0.0056	0.73	539.1	194.9	-	0.4	584.9	96.7	132.3	7
HS16-4	296.9	105.8	0.142	0.0118	0.81	446.0	142.9	-	0.3	479.6	87.2	104.8	6
HS19-1	268.9	100.5	23.788	0.0082	0.79	225.1	104.5	-	0.5	249.6	94.6	119.0	7
HS19-2	236.4	77.0	34.067	0.0044	0.75	622.6	193.3	-	0.3	668.0	93.9	125.8	7
HS19-3*	216.7	88.0	36.371	0.0052	0.76	423.5	242.9	-	0.6	480.6	119.0	156.6	9
HS19-4	266.8	118.0	25.717	0.0120	0.82	180.0	83.1	-	0.5	199.5	87.6	106.8	6

[a] FT is the a-ejection correction after Farley et al. (1996).

[b] Weighted mean age calculated using IsoplotR of Vermeesch (2018).

[c] Effective Uranium content, [eU]=[U]+0.235 × [Th] (Flowers et al., 2009).

* Excluded in calculating weighted age using IsoplotR (Vermeesch et al., 2018).